Calibrated Passive Microwave Daily *EASE-Grid 2.0* Brightness Temperature ESDR (CETB)

Algorithm Theoretical Basis Document
Version 2.0
June 14, 2023

Mary J. Brodzik[1], David G. Long[2] and Molly A. Hardman[1]

[1] *National Snow and Ice Data Center, Cooperative Institute for Research in Environmental Sciences, University of Colorado, 449 UCB, Boulder, CO, 80309-0449, USA*
[2] *Microwave Earth Remote Sensing Laboratory, Brigham Young University, Provo, UT, USA*

Contents

List of Figures

List of Tables

1 ATBD Revision History

Table 1: *ATBD Revision History*

Revision	Date	Purpose
0.5	2014-04-30	Initial Revision
0.6	2014-06-18	Figure 2 and 4 placeholders replaced
		Quantified EIA drift in Appendix 10.1
		New note about CSU vs. RSS orbit definitions
		Added Appendix 10.5 "Comparison of Heritage Data Sets with CETB ESDR"
0.7	2014-06-19	Section 6.2.2.2: clarified statements on effective resolution
		Appendix 10.2: clarified/expanded (sensor) measurement response function (MRF) terminology
		Added new Section 10.2.9: "Local Time-of-Day Analysis"
		Minor formatting corrections
0.8	2014-08-05	Corrected EASE2_T grid dimensions
		Minor formatting and grammatical corrections
		Corrected figure/table cross-references
0.9	2015-02-10	Deleted placeholder paragraph in 4.2.1 with reference to discussion in Section 8.3
		Changed Section level of ltod from 8.2.9 to 8.3
		Added placeholder sample images
0.10	2015-06-05	Inserted Section 2.1 "Project Purpose"
		Section 3.2.3 Output Data: corrected reference to CF conventions
		Table 3-3: update FCDR field requirements
		Section 3.2.3.1: clarified description of TB file contents
		Appendix 8.6: replaced TBD items with actual references, added row describing image reconstruction tuning parameters
		Inserted references to recent project white papers
		Added Appendix describing end-to-end swath overlap
		Added Appendix with Abbreviation and Acronym list
		Updated Appendix with CETB format definitions and filename conventions
0.11	2016-02-12	Corrected typos and references in EFOVs for SSM/I and AMSR-E
		Addressed various reviewer comments

		Finalized some (originally TBD) implementation details
		Made equations labeling consistent throughout document and appendices
		Combined separate appendix reference lists into one for all appendix material
		Replaced DRAFT CETB file CDL with actual CDL describing prototype v0.1 file format
1.0	2018-04-26	This version of ATBD is finalized as Brodzik and Long (2018) and applies to CETB v1.3 to v1.5 files
		Finalized Appendix information with implementation details, including latest ltod values used
		Corrected/finalized TBD items throughout
		Included final details for Storage Requirements
		Made biblography formatting consistent throughout
2.0	2023-06-14	Major revision for data set CETB v2.0 (nsidc0630v2) modifications
		Removed v1 sections that do not apply to CETBv2 processing
		All sections revised/updated/reorganized

2 CETBv2 Product Update Summary

Table 2 contains significant changes implemented to update CETB production for Version 2 data release.

Table 2: *CETBv1 vs. CETBv2 Product differences*

	CETBv1	CETBv2	Section
Sensors	SSM/I (6), SSMIS (4), AMSR-E, SMMR	Same as v1, added AMSR2	5
Input	SSM/I-SSMIS: CSU FC-DRv1	SSM/I-SSMIS: GPM L1C	5, E, C
	AMSR-E: RSS	AMSR-E: GPM L1C + JAXA L1B	
	AMSR2: n/a	AMSR2: GPM L1C + JAXA L1B	
	SMMR: SMMR Pathfinder	Same as v1	
Filenames	Longer filenames	Shorter filenames, conform to latest DAAC standards	D.2
Conventions	CF-1.6	CF-1.9	D, C.9
Algorithms	GRD and rSIR	Same as v1	6

3 Purpose of this Document

This document is the algorithm theoretical basis for the Calibrated Passive Microwave Daily EASE-Grid 2.0 Brightness Temperature (CETB) Earth System Data Record (ESDR) product. The CETB product is generated from calibrated swath brightness temperature (TB) data at the National Snow and Ice Data Center (NSIDC) NASA Distributed Active Archive Center (DAAC), using image reconstruction algorithms originally developed at Brigham Young University (BYU) and further refined at NSIDC for application to the current suite of sensors (Long and Brodzik, 2016). The CETB product is archived and available to the public as data set ID nsidc0630 from the NSIDC DAAC (Brodzik et al., 2023). The NSIDC DAAC currently supports near real-time (NRT, ~1 day latency from observation) processing of CETB for ongoing operational sensors. The current CETB release is v2.0.

This ATBD has been revised significantly to reflect changes between CETB v1.x and v2.x data set processing. Sections from the ATBD v1.0 (Brodzik and Long, 2018) that are no longer applicable to CETB v2.0 data have been removed. Several theoretical sections have been revised and moved from the Appendices to the algorithm description in the main document. This ATBD v2.0 is applicable to CETB v2.x data. CETB v2.x data should be treated as an improved data set that completely replaces CETB v1.x. Users are encouraged to discontinue use of CETB v1.x data, which will be discontinued when all data have been reprocessed as CETB v2.0. Throughout this document, the data are referenced without a version number when the topic applies to both v1.x and v2. References with version numbers are used when the topic only applies to the specified version.

This document includes the following sections: Section 3 describes the purpose of this ATBD. Section 4 introduces major changes incorporated into Version 2 of the data set. The input swath data are described in Section 5. Section 6 contains the theoretical background and algorithm description for the image reconstruction techniques used to produce CETB grids. Section 7 contains the CETB v2.x product description, including grid and spatial resolution details, sample images, product data volumes. Section 8 includes acknowledgements for agencies and resources that funded the development and production of the CETB data product. Several appendices are included with tabular and implementation details. An acronym list is included in Appendix F.

4   Introduction

The Calibrated EASE-Grid 2.0 Brightness Temperature (CETB) Earth Science Data Record (ESDR) product is a multi-sensor, gridded data set incorporating over 45 years of passive microwave observations from SMMR, SSM/I-SSMIS, AMSR-E and AMSR2 sensors (Figure 1). Version 2 processing (CETBv2) incorporates the latest available swath inputs, the Global Precipitation Mission (GPM) Level 1C (L1C) products (Berg et al., 2018), which implement a more stable cross-sensor calibration and include AMSR-E and AMSR2. Like CETBv1 (Brodzik et al., 2016), the current reprocessing uses CF-compliant, netCDF file structures, high quality control, file-level provenance, EASE-Grid 2.0 grid definitions (Brodzik et al., 2012, 2014), and local time-of-day processing. The CETB ESDR includes conventional resolution products as well as enhanced-resolution imagery derived from the computationally efficient radiometer version of Scatterometer Image Reconstruction (rSIR). The CETBv2 product supercedes the CETBv1 product. This ESDR serves the land surface and polar snow and ice communities that use gridded passive microwave data in long-term climate studies.
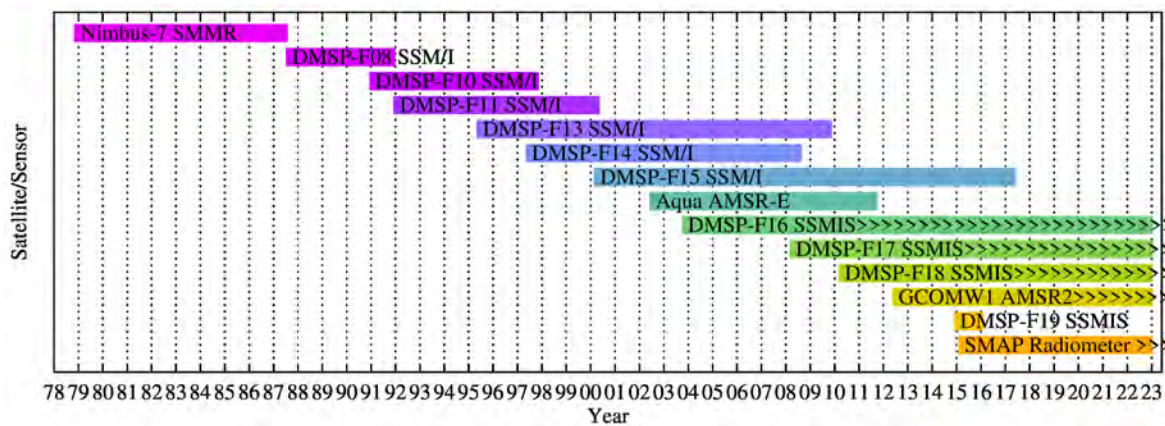
Figure 1: *Time series of CETBv2 passive microwave sensors. Sensors labeled with "»" are still operating as of June 2023. Dates are approximate. Compatible SMAP CETB data are distributed as a separate data set (Brodzik et al., 2021).*

5   Input Data Sets

To avoid amplification of noisy signals in the image reconstruction process, the CETB processing depends on input data with the lowest noise possible. Minimum requirements for input swath data for image reconstruction are listed in Table 3.

Table 3: *CETB Input Swath Data Requirements.*

Variable	Characteristics	Requirement
Geolocation (lat/lon)	By measurement	Position of the center of each measurement footprint (decimal degrees)
T_B	By measurement	Needed for all output methods (Kelvins)
Earth incidence angle	By measurement	Needed by CETB derived product users for potential T_B adjustment (Degrees from vertical)
Earth azimuth angle	By measurement	Needed for image reconstruction (Degrees from North) Can be calculated from spacecraft position and measurement position
Measurement quality	By measurement	Quality indicator flag; determines whether T_B is used for image reconstruction
Spacecraft position	By scan line[1]	Needed for image reconstruction (Meters, spacecraft reference frame North, East, Down (NED))
Measurement time	By scan line[1]	Needed for output time variable (Seconds)

CETB v2 input swath brightness temperatures include the data sets in Table 4. A relative timeline of included sensors is depicted in Figure 1.

---

[1]Data must be updated at a sufficiently high rate that quadratic interpolation can be used to derive data between updates.

Table 4: *CETB v2 Input Data Sets*

Sensor	Years	Input Data	Channels	Reference
SMMR	1978–1987	Nimbus-7 SMMR Pathfinder TBs	all	(Njoku, 2003)
SSM/I-SSMIS	1987–present	GPM L1C FCDR	all	(Berg et al., 2018)
AMSR-E	2002–2011	JAXA L1B	(unresampled) 6 GHz	(Maeda et al., 2016)
AMSR-E	2002–2011	GPM L1C FCDR	10–89 GHz	(Berg et al., 2018)
AMSR2	2012–present	JAXA L1B	(unresampled) 6 GHz	(Maeda et al., 2016)
AMSR2	2012–present	GPM L1C FCDR	10–89 GHz	(Berg et al., 2018)

5.1   PPS L1C

Input swath data for all SSM/I, SSMIS and most frequencies (all but 6 GHz) of AMSR-E and AMSR2 sensors are obtained from the Global Precipitation Mission (GPM) Level 1C (L1C) Fundamental Climate Data Record (FCDR) (Berg et al., 2018), distributed by the NASA Precipitation Processing System (PPS). The L1C data include a 35+ year intercalibrated data record from 14 research and operational conical-scanning microwave imagers. L1C data are obtained from the NASA Precipitation Processing System (PPS) at `https://pmm.nasa.gov/data-access/downloads/gpm`. Subject to extensive quality-control procedures and cross-scan bias and geolocation corrections, the L1C data are calibrated using the GPM GMI instrument as the calibration reference. Berg et al. (2018) consider GMI to be an excellent absolute calibration reference due to the instrument design and post-launch calibration analysis. This choice of input data source replaces the CSU FCDRv1 that were used as input to CETBv1. Some unavoidable cross-sensor differences remain due to variations in channel frequencies, polarization, spectral band width and view angles.

5.2   JAXA L1B

Due to GPM calibration requirements and agreements with data providers of the L1B products, 6 GHz data from both AMSR-E and AMSR2 are not included in the L1C FCDRs. These channels are not used in GPM precipitation products and are therefore omitted from L1C production (E. Stocker, personal communication, 20 Oct 2021). For CETBv2 processing, input swath data for 6 GHz channels from AMSR-E and AMSR2 are obtained from JAXA L1B data (Maeda et al., 2016).

5.3   SMMR Pathfinder

The Nimbus-7 Scanning Multichannel Radiometer (SMMR) instrument is unavailable from the L1C FCDR. Input swath data for SMMR are obtained from Nimbus-7 SMMR Pathfinder Brightness Temperatures (Njoku, 2003). These input data are unchanged from the inputs used to produce CETB v1.0. CETB data for the SMMR sensor are therefore the only data that are substantively unchanged from CETBv1 to CETBv2.

6   Reconstruction Theory

6.1   Theory of Reconstruction and Gridding Algorithms

All algorithms to transform radiometer data from swath to gridded format are characterized by a tradeoff between noise and spatial resolution. The CETB processing includes both low-noise (low-resolution) gridded data and enhanced-resolution data grids, with potentially higher noise, to enable product users to compare and choose which option better suits a particular research application.

All radiometer channels in the CETB product are gridded to the coarsest resolution (25 km) grids using the GRD drop-in-the-bucket method. This produces gridded data with the smoothest, lowest noise possible, at the expense of resolution. All channels are also gridded at enhanced resolutions using the rSIR method, on nested grids at power-of-2 divisors of the base 25 km grid. This produces images with higher spatial detail, with potentially greater noise (Figures 2, 3 and 4).

The following sections describe the theoretical basis for reconstruction and gridding.

6.2   GRD Algorithm

The CETB coarse resolution gridding procedure is a simple, "drop-in-the-bucket" (unweighted) average. The resulting data grids are designated GRD data arrays. For the drop-in-the-bucket gridding algorithm, the key information required is the center location of the measurement. The center of each swath geolocation is mapped to an output projected grid cell. All measurements within the specified time period with center locations within the bounds of a particular grid cell are averaged (Figure 2). This is the reported T_B value for this pixel. Ancillary variables contain the number and standard deviation of included samples.

6.3   rSIR Algorithm

6.3.1   Background Theory

Microwave radiometers measure the thermal emission, sometimes called the Plank radiation, radiating from natural objects (Ulaby and Long, 2014). In a typical radiometer, an antenna is scanned over the scene of interest and the output power from the carefully calibrated receiver is measured as a function of scan position. The reported signal is a temporal average of the filtered received signal power.

The observed power is related to the receiver gain and noise figure, the antenna loss, the physical temperature of the antenna, the antenna pattern, and the scene brightness temperature (Ulaby and Long, 2014). In simplified form, the output power P_{SYS} of the

25 km

GRD (25 km):
pixel TB is average of measurements
whose center location falls inside the
pixel area

25 km

rSIR (3.125 km):
each pixel TB derived from all
overlapping measurements,
weighted by antenna gain
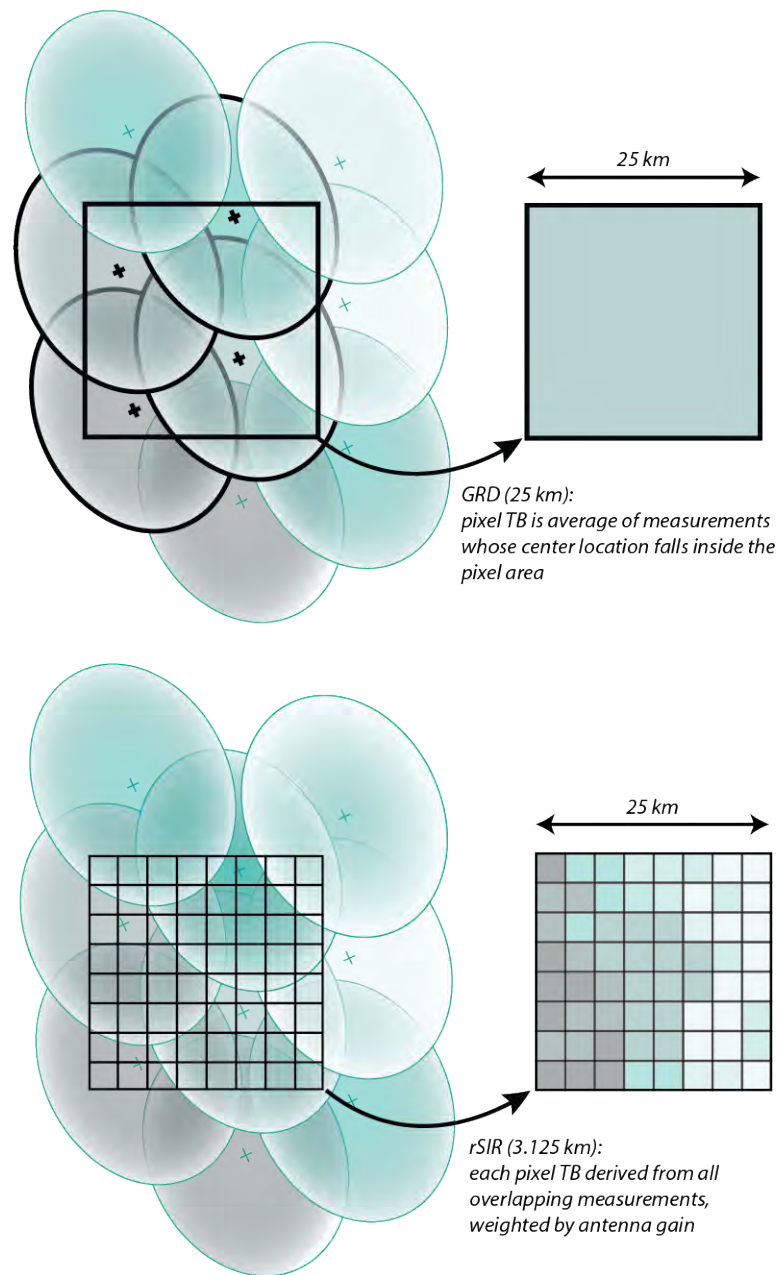
Figure 2: *Gridding techniques (top) with the lowest noise factors take the average of all measurements whose locations fall inside the gridded pixel area, producing smooth but relatively coarse-resolution output. Compare to image reconstruction for resolution enhancement (bottom), which takes advantage of oversampled information in overlapping brightness temperature footprints to deduce higher-resolution gridded output.*
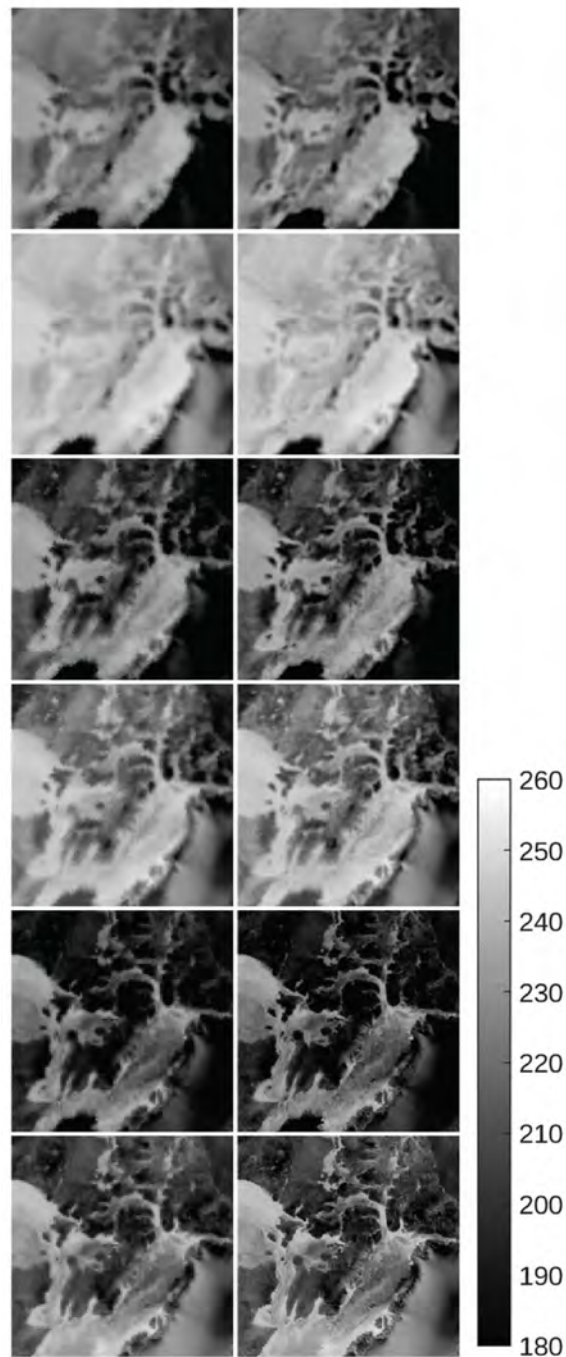
Figure 3: *Subimages extracted from daily CETB Northern Hemisphere SSM/I CETB product: (Left) GRD, (Right) rSIR, and for channels (Rows, top to bottom) 19H, 19V, 37H, 37V, 85H and 85V. The zoomed area spans 250 km x 250 km, centered over Baffin Island west of Greenland, which is partially visible in the lower right corner (Long and Brodzik, 2016)*
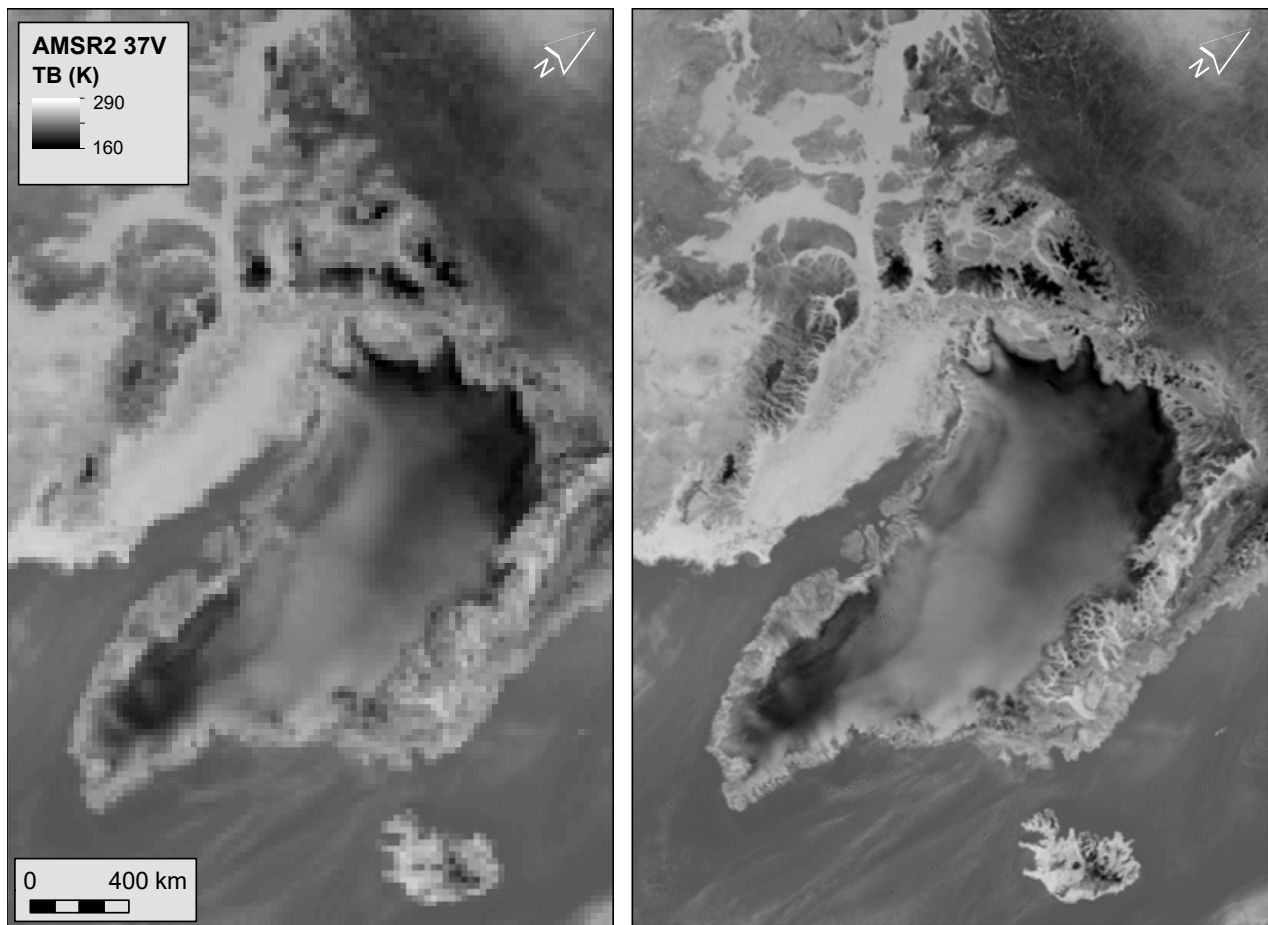
Figure 4: *CETBv2 data at conventional vs. enhanced-resolution, Greenland, 04 Dec 2022, showing improved capability to resolve variability at sea ice edges and coastal fjords: AMSR2 37 GHz, vertically-polarized, CETB GRD (25 km, left) vs. enhanced-resolution rSIR (3.125 km, right) (Hardman et al., 2022)*

receiver can be written as

$$P_{SYS} = k\,T_{SYS}\,B \tag{1}$$

where $k = 1.38 \times 10^{-28}$ is Boltzmann's constant, B is the receiver bandwidth and T_{SYS} is the system temperature, defined as

$$T_{SYS} = \eta_1 T_A + (1 - \eta_1)T_p + (L - 1)T_p + LT_{REC} \tag{2}$$

where η_1 is the antenna loss efficiency, T_p is the physical temperature of the antenna and waveguide feed, L is waveguide loss, T_{REC} is the effective receiver noise temperature (determined by system calibration), and T_A is the effective antenna temperature. As described below, T_A is dependent on the direction the antenna points and the scene characteristics. Since the other instrument-related terms (i.e., $(1 - \eta_1)T_p + (L - 1)T_p + LT_{REC}$) are approximately constant, T_{SYS} is dominated by T_A, which depends on the geophysical parameters of interest.

The effective antenna temperature, T_A, can be modeled as a product of the apparent temperature distribution $T_{AP}(\theta, \varphi)$ in the look direction (θ, φ) (see Figure 5) and the antenna radiation gain $F(\theta, \varphi)$, which is proportional to the antenna gain pattern $G(\theta, \varphi)$ (Ulaby and Long, 2014). T_A (in K) is obtained by integrating the product of apparent temperature distribution $T_{AP}(\theta, \varphi)$ (in K) and the antenna pattern $G(\theta, \varphi)$

$$T_A = G_a^{-1} \iint G_i(\theta, \varphi)\,T_{AP}(\theta, \varphi)\,d\theta d\varphi \tag{3}$$

where

$$G_a = \iint G_i(\theta, \varphi)\,d\theta d\varphi \tag{4}$$

$G_i(\theta, \varphi)$ is the instantaneous antenna gain for the particular channel and the where the integral domain is the range of values corresponding to the non-negligible gain of the antenna. Note that the antenna pattern acts as a low pass spatial filter of the surface brightness distribution, limiting the primary surface contribution to the observed T_B to approximately the 3 dB beamwidth. The observed value can be split into contributions from the mainlobe and the sidelobes,

$$T_A = \eta_M\,T_{ML} + (1 - \eta_M)\,T_{SL} \tag{5}$$

where η_M is the main lobe efficiency factor defined as

$$\eta_M = G_a^{-1} \iint_{mainlobe} G_i(\theta, \varphi)\,d\theta d\varphi \tag{6}$$
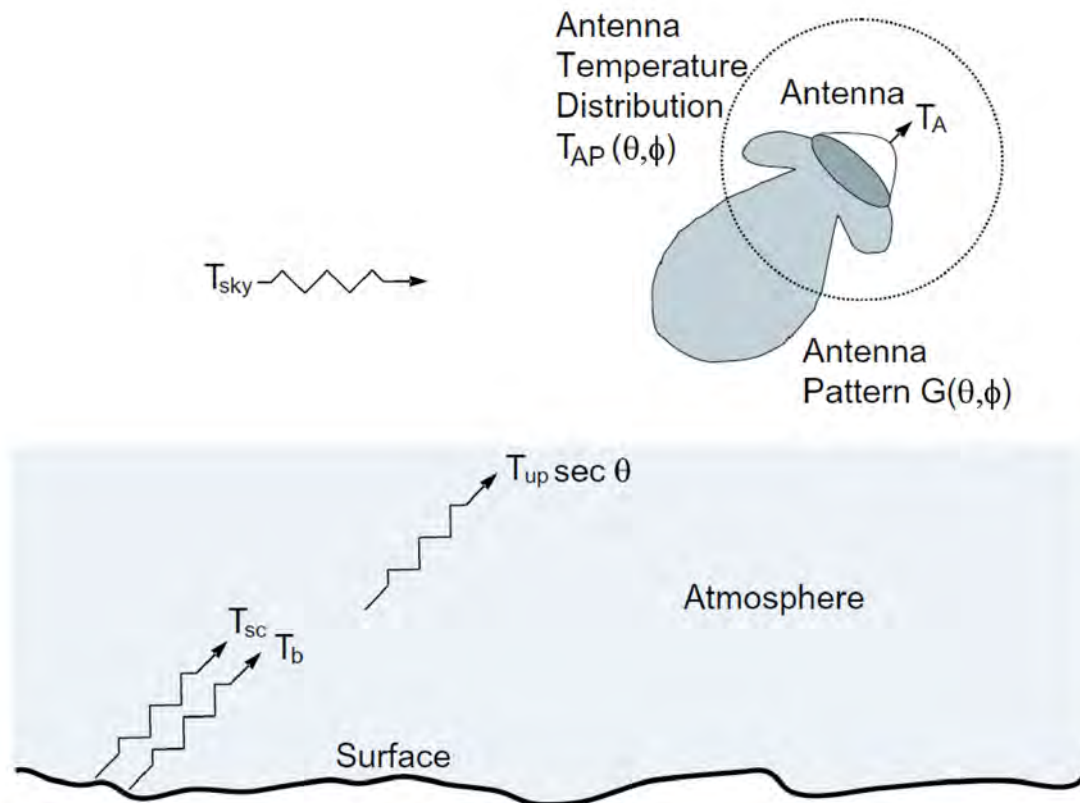
Figure 5: *The apparent temperature distribution as seen by the radiometer antenna. The antenna temperature T_A is the normalized integral of the product of the temperature distribution and the antenna gain pattern. The apparent temperature of the surface seen through atmosphere includes the upwelling radiation, T_{up}, from the atmosphere plus the attenuated surface brightness temperature, T_B, and the surface scattered brightness temperature, T_{SC}. Brightness temperature contributions from extra-terrestrial sources are grouped in T_{sky}.*

where the integral is over (only) the main lobe of the antenna and

$$T_{ML} \;=\; G_a^{-1} \iint_{mainlobe} G_i(\theta, \varphi)\, T_{AP}(\theta, \varphi)\, d\theta d\varphi \tag{7}$$

$$T_{SL} \;=\; G_a^{-1} \iint_{sidelobes} G_i(\theta, \varphi)\, T_{AP}(\theta, \varphi)\, d\theta d\varphi \tag{8}$$

For downward-looking radiometers, the apparent brightness temperature distribution includes contributions from the surface and the intervening atmosphere (Ulaby and Long, 2014). For a spaceborne sensor this can be expressed as

$$T_{AP}(\theta, \varphi) \;=\; [\, T_B(\theta, \varphi) \,+\, T_{SC}(\theta, \varphi) \,]\, e^{-\tau \sec \theta} \,+\, T_{up}(\theta) \tag{9}$$

where $T_B(\theta, \varphi)$ is the surface brightness temperature, $T_{SC}(\theta, \varphi)$ is the surface scattering temperature, τ is the total effective optical depth of the atmosphere and $T_{up}(\theta)$ is the effective atmospheric upwelling temperature. T_{up} is the effective radiometric temperature of the atmosphere, which depends on the temperature and density profile, atmospheric losses, clouds, rain, etc.

Ignoring incidence and azimuth angle dependence, the surface brightness temperature is

$$T_B \;=\; \epsilon\, T_P \tag{10}$$

where ϵ is the emissivity of the surface and T_P is the physical temperature of the surface. The emissivity is a function of the surface roughness and the permittivity of the surface, which are related to the geophysical properties of the surface (Ulaby and Long, 2014). In geophysical studies, the key parameter of interest is ϵ or T_B.

The surface brightness temperature, $T_{SC}(\theta, \varphi)$, is the result of downwelling atmospheric emissions which are scattered off the rough surface toward the sensor. This signal depends on the scattering properties of the surface (surface roughness and dielectric constant) as well as the atmospheric emissions directed toward the ground. Note that azimuth variation with brightness temperature has been observed over the ocean (Wentz, 1992), sand dunes (Stephen and Long, 2005), and snow in Antarctica (Long and Drinkwater, 2000). Vegetated and sea ice-covered areas generally have little or no azimuth brightness variation.

6.3.2   Signal Integration

The received signal power is very noisy. To reduce the measurement variance, the received signal power is averaged over a short "integration period." Even so, the reported measurements are noisy due to the limited integration time available for each measurement. The uncertainty is expressed as ΔT, which is the standard deviation of the temperature measurement. ΔT is a function of the integration time and bandwidth used to make the radiometric measurement and is typically inversely related to the time-bandwidth product

(Ulaby and Long, 2014). Increasing the integration time and/or bandwidth reduces ΔT. High stability and precise calibration of the system gain is required to accurately infer the brightness temperature T_B from the sensor power measurement P_{SYS}.

Because the antenna is scanning during the integration period, the effective antenna gain pattern of the measurements is a smeared version of the antenna pattern. In the smeared case, we replace G_i in Equation 3 and Equation 4 with the "smeared" version of the antenna, G_s where

$$G_s(\theta, \varphi) \;=\; T_i^{-1} \int G_i(\theta, \varphi \,+\, \Delta\varphi t)dt \tag{11}$$

where T_i is the integration period, $\Delta\varphi$ is the rotation rate, and the integral limits are $-T_i$ and 0. Note that because T_i is very short, the net effect is primarily to widen the main lobe. Nulls in the pattern tend to be eliminated and the sidelobes are widened. Note that the smeared antenna pattern may vary somewhat for different antenna azimuth angles, though we do not consider this effect here.

Because the antenna pattern has been specifically designed to minimize the power from directions not from the surface, we can neglect the antenna smearing from non-surface contributions and concentrate on the pattern smearing at the surface. The smeared antenna pattern $G_s(\theta, \varphi)$ at the surface at a particular time defines the "spatial measurement response function" (MRF) of the corresponding T_B measurement.

Note from Equation 9 that $T_{AP}(\theta, \varphi)$ consists primarily of an attenuated contribution from the surface (i.e., T_B) plus scattered and upwelling terms (Figure 5). We note that the reported T_A values compensate or correct (to some degree) for these terms. Also, T_A is measured over an array of points. Let T'_A denote the corrected T_A measurement. It follows that we can re-write Equation 9 in terms of the corrected T_A and the surface T_B value as

$$T'_A \;=\; G_a^{-1} \iint G_s(\theta, \varphi) \, T_B(\theta, \varphi) \, d\theta d\varphi \tag{12}$$

We can express this result in terms of the surface coordinates x and y as (noting that for a given (x, y) location and time, the antenna elevation and azimuth angles can be computed)

$$T'_A \;=\; G_b^{-1} \iint G_s(x, y) \, T_B(x, y) \, dxdy \tag{13}$$

where

$$G_b \;=\; \iint G_s(x, y) \, dxdy \tag{14}$$

We define the MRF to be

$$R(x, y) \;=\; G_b^{-1} \, G_s(x, y) \, dxdy \tag{15}$$

so that

$$T'_A = \iint R(x,y)\, T_B(x,y)\, dxdy \tag{16}$$

The measurements T'_A can therefore be seen to be the integral of the product of the MRF and the surface brightness temperature.

The "nominal" resolution of the T'_A measurements is considered to be the size of the 3 dB response pattern of the MRF. Our goal is to estimate $T_B(x,y)$ from the measurements T'_A at the various sample locations.

6.3.3 Spatial Measurement Response Function

In reconstruction algorithms, the effective measurement response function (MRF) is used. As described in the previous section, the MRF is determined by the antenna gain pattern (which is unique for each sensor and sensor channel, and may vary with scan angle), the scan geometry (notably the antenna scan angle), and the integration period. The latter "smears" the antenna gain pattern due to antenna rotation over the measurement integration period. The MRF describes how much the emissions from a particular receive direction contribute to the observed T_B value.

Denote the MRF for a particular channel by $R(\varphi, \theta; \phi)$ where φ and θ are particular azimuth and elevation angles, while ϕ is the scan angle (sometimes referred to as the antenna azimuth angle). Note that for a given scan angle the integral of R over all the azimuth and elevation angles is 1. Generally, for the FCDRs that are input to the CETB, the MRF can be treated as zero everywhere but in the direction of the surface. With this assumption, we can write $R(\varphi, \theta; \phi)$ as $R(x,y; \phi)$ where x and y are the location (which we express in map coordinates) on the surface corresponding to the azimuth and elevation angles. Note that:

$$\iint_{surface} R(x,y; \phi_i)dxdy = 1 \tag{17}$$

Then, a particular measurement T_i can be written as

$$T_i = \iint_{surface} R(x,y; \phi_i)T_B(x,y; \phi_i)dxdy \tag{18}$$

where the scan angle ϕ_i corresponds to the scan angle at the center (or start) of the integration period and $T_B(x,y; \phi_i)$ is the nominal brightness temperature in the direction of point (x,y) on the surface as observed from the scan angle position. Note that if there is no significant difference in the atmospheric contribution as seen from different scan angles, we can treat $T_B(x,y; \phi_i)$ as independent of ϕ_i so that $T_B(x,y; \phi_i) = T_B(x,y)$. For convenience $T_B(x,y)$ is referred to as the surface brightness temperature.

With this approximation, we can write Equation 18 as:

$$T_i = \iint_{surface} R(x, y; \phi_i) T_B(x, y) dx dy \tag{19}$$

Each T_B measurement is seen to be the MRF-weighted average of T_B. The goal of the reconstruction algorithm is to estimate $T_B(x, y)$ from the measurements T_i.

In the following, we present a signal processing approach to infer the surface brightness temperature. Based on Long and Brodzik (2016), we treat the surface brightness temperature as a two-dimensional signal to be estimated from irregular samples (the measurements). Some heritage products used an alternative least-squares approach based on the Backus and Gilbert (1967). Both approaches enable estimation of the surface brightness on a finer grid than possible with the GRD approach, i.e., the resulting brightness temperature estimate has a finer effective spatial resolution than the GRD approach. The results are often called "enhanced resolution," although reconstruction algorithms merely exploit the available information to reconstruct the original signal at higher resolution than gridding under the assumption of a band-limited signal (Early and Long, 2001). The resolution enhancement possible compared to the GRD product depends on the sampling density and the MRF; however, improvements in the effective resolution of 30–60% over GRD methods have been demonstrated in practice (Long et al. (2021) and Long et al. (2023)). In order to meet Nyquist requirements for the signal processing, the pixel resolution of the images must be finer than the effective resolution by at least a factor of two.

For comparison, the effective resolution for drop-in-the bucket (GRD) gridding is the grid size plus the spatial dimension of the measurement (3 dB beamwidth). Reconstruction processing can be implemented to yield higher effective resolution. Reconstruction processing does correlate adjacent fine resolution pixels; the effective spatial resolution of rSIR images is coarser then the pixel dimension, but finer than the GRD products.

In the polar regions, multiple passes over the same area are frequently averaged together. Reconstruction algorithms intrinsically exploit the resulting oversampling of the surface to improve the effective spatial resolution in the final image.

6.3.4 Signal Reconstruction

In the signal processing approach to image reconstruction, $T_B(x, y)$ is treated as a noisy two-dimensional signal to be estimated from the measurements T_i. For practical reasons, $T_B(x, y)$ is treated as a discrete signal sampled at the map pixel spacing. This spacing must be set sufficiently fine so that the generalized sampling requirements (Gröchenig, 1992) are met for the signal and the measurements (Early and Long, 2001). Typically, this is one-fifth to one-tenth the size of the antenna footprint size. The product is posted at this fine resolution even though the effective resolution of the enhanced resolution images is coarser than the pixel dimension.

Let $T_B(x, y)$ be the discrete brightness temperature we are attempting to estimate. For convenience we vectorize this two-dimensional signal over an N_x by N_y pixel grid into a single dimensional variable a_j where:

$$a_j \;=\; T_B(x_l, y_k) \tag{20}$$

where $j = l + N_x j$. The measurement equation, Equation 19, becomes

$$T_i \;=\; \sum_{j \in image} h_{ij} a_j \tag{21}$$

where $h_{ij} = R(x_l, y_k; \phi_i)$ is the discrete measurement response function (MRF) for the ith measurement evaluated at the pixel center and the summation is over the image. We require that the discrete MRF be normalized so that

$$1 \;=\; \sum_{j \in image} h_{ij} \tag{22}$$

In practice, the MRF is negligible some distance from the measurement so this sum need only be computed over an area local to the measurement position. Some care has to be taken near image boundaries.

For the collection of available measurements, Equation 21 can be written as the matrix equation

$$\vec{T} \;=\; \mathbf{H}\vec{a} \tag{23}$$

where $\mathbf{H}$ contains the sampled MRF for each measurement. Note that $\mathbf{H}$ is (very) large, sparse, and may be underdetermined.

Estimating the brightness temperature is equivalent to inverting Equation 23. While a variety of approaches to this have been proposed, in practice, due to the large size of $\mathbf{H}$, iterative methods are used. One advantage of an iterative method is that regularization can be easily implemented by prematurely terminating the iteration; otherwise an explicit regularization method can be used.

The radiometer form of the Scatterometer Image Reconstruction (rSIR) is a particular implementation of an iterative solution to Equation 23 that has proven effective in generating high resolution brightness temperature images (Long and Daum, 1998). The rSIR estimate approximates a maximum-entropy solution to an underdetermined equation and least-squares to an overdetermined system. rSIR provides results similar to the Backus/Gilbert, but with significantly less computation (Long and Brodzik, 2016).

For implementation in the CETB, fine map grid resolutions were selected for each channel according to Table 5.

Table 5: *CETB Fine Resolution Grids*

Frequencies (GHz)	Fine Grid Scale Factor	Fine Grid Resolution (km)
< 18	2	12.5
$18 - 22$	4	6.25
> 22	8	3.125

For CETB products, we are following Long and Daum (1998) to define "nearby" for most sensors and channels as regions where the MRF is within 8 dB of the peak response (some exceptions are described in Appendix C.7). We compute the solution separately for each output pixel using the particular measurement geometry antenna pattern at the swath location and scan angle rotation. Figure 26 illustrates the variation in SSM/I antenna gain patterns (which are closely related to the MRF) with location over the swath. The other sensors are similar. This significantly increases the computational load, but results in the best quality images.

6.4 rSIR Performance from Simulation

As described in Long and Brodzik (2016), we used simulation to evaluate the rSIR algorithm, and to evaluate tradeoffs in selecting algorithm parameters for output pixel size and number of iterations. We evaluated results of the iterative rSIR method compared to the matrix inversion Backus-Gilbert (BG) method. We define a simplified, but still realistic, simulation of the sensor geometry using an idealized MRF to generate measurements of a synthetic, Earth-centered image (Figure 6). Using noisy and noise-free measurements, we created GRD, AVE, rSIR, and BG images, with error (mean, and root-mean-square [rms]) determined for each case. The measurements were assumed to have a standard deviation of $\pm 1\,\mathrm{K}$; results were relatively insensitive to the standard deviation value used. The same simulated measurements were used for both BG and rSIR.

We analysed the rSIR reconstruction accuracy relative to the accuracy of the MRF, determining that, when used for only partial reconstruction, rSIR is tolerant to errors in describing the MRF. We use a simplified MRF model, based on a 2-D Gaussian function whose $3\,\mathrm{dB}$ (half-power) matches the footprint size (see further details in Appendix C.2). During processing, the orientation of the ellipse is rotated at each measurement. The MRF is positioned at the center of the nearest neighbor pixel to the measurement location and oriented to align with the azimuth antenna angle. The values of the discrete MRF are then computed at the center of each pixel in a box surrounding the pixel center. The size of the box is defined to be the smallest enclosing box for which the sampled antenna pattern is larger than a minimum gain threshold, relative to the peak gain. Box sizes by sensor and
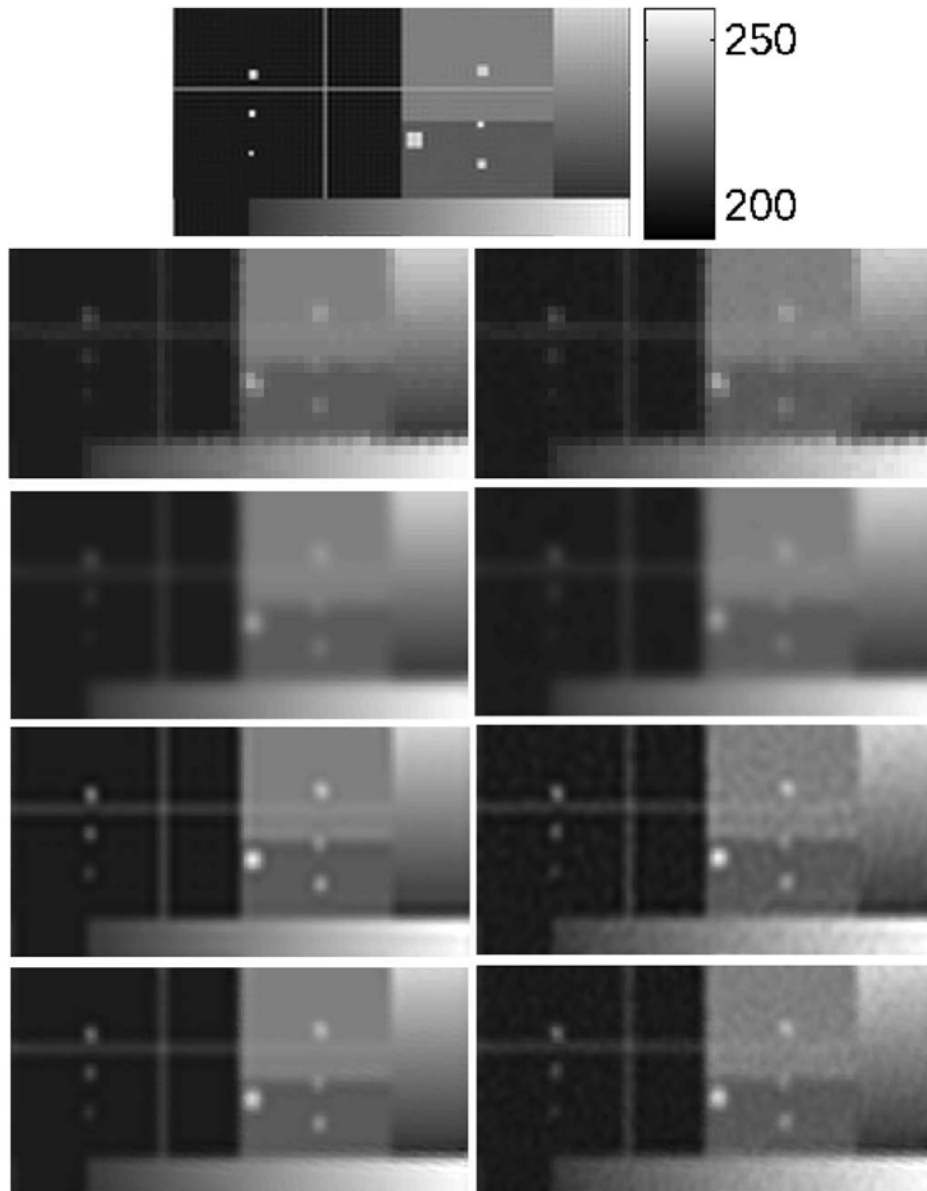
Figure 6: *SSM/I 37 GHz T_B image simulations from different methods. (Top Panel) "True" simulation image. (Left Column) Noise-free simulation results. (Right Column) Noisy simulation results. (Top Row) 25 km GRD. (Second Row) AVE (rSIR for iteration = 1). (Third Row) rSIR for iteration = 20). (Bottom Row) Backus Gilbert (BG) ($\gamma = 0.85\ \pi$). (Long and Brodzik, 2016).*

channel are included in Table 16 and are recorded in each file in the `TB` variable-level attribute, `measurement_search_bounding_box_km`. The minimum gain threshold is recorded in the `TB` variable-level attribute, `measurement_response_threshold_dB`.

The image pixel size defines how well the MRF can be represented in the reconstruction processing and the simulation. Figure 7 illustrates representative plots of the MRF sampling for each pixel size under consideration, relative to the 25 km base grids. As the pixel size is decreased, the sampled MRF more closely resembles a continuous MRF, thereby reducing quantization error; however, smaller pixel sizes increase computational load and the size of output products. Finer resolution results in smoother images on a finer posting grid. To meet Nyquist requirements, image results must be posted at least twice the highest frequency component of the signal.
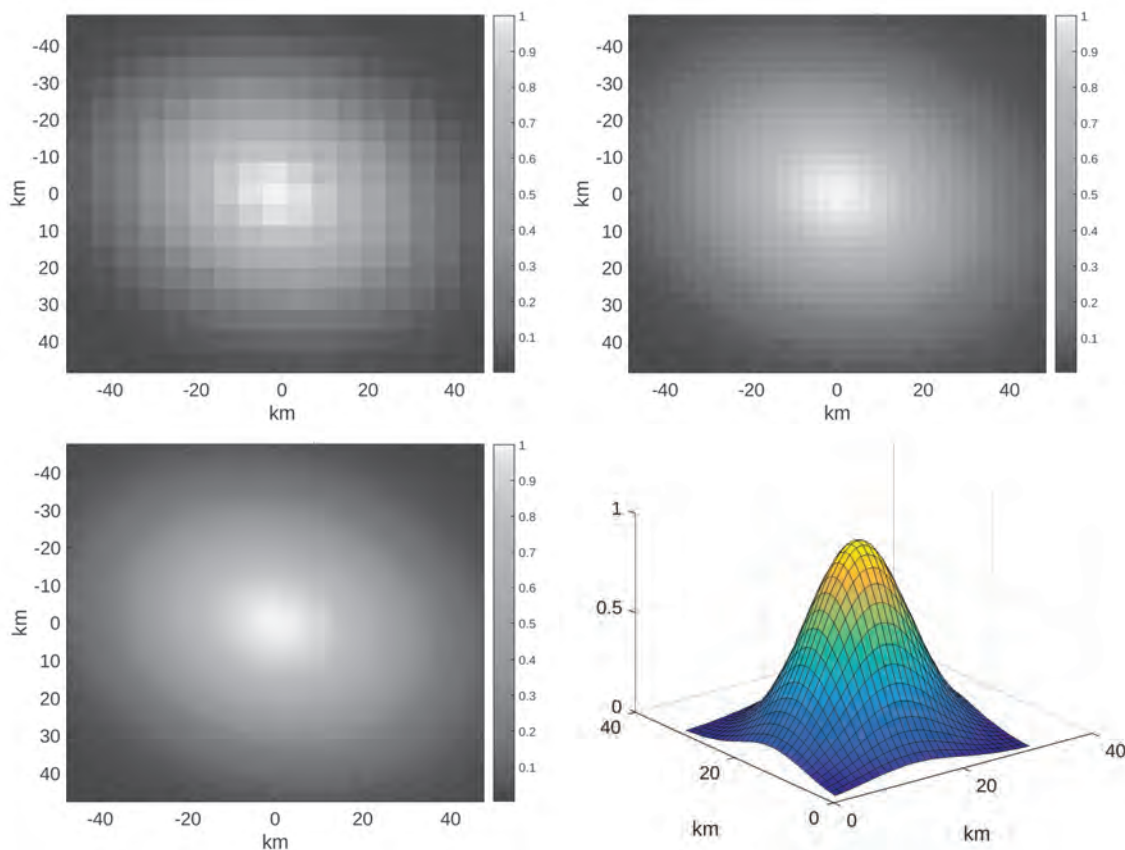

Figure 7: *Sampled MRF plots for potential reconstruction pixel sizes relative to 25 km base grids: 6.25 km (top left), 3.125 km (top right), 1.5625 km (bottom left), with perspective view of 3.125 km MRF (bottom right) (Long et al., 2019).*

Two pass cases were evaluated: a single-pass case and a case with two overlapping

passes. The simulation showed that the relative performance of rSIR and BG was the same for both cases. As expected, simulation results improve for dual-pass cases. For most cases, the simulation error is effectively zero mean. For all cases, multiple passes have the smaller error. This leads to the more generalized observation that, for sun-synchronous orbits, the quality of image reconstruction generally improves near the poles, where multiple overlapping orbit passes are available.

Long and Brodzik (2016) also demonstrated the tradeoff between reconstruction accuracy and noise, noting that truncation of the rSIR iteration is useful minimize overall error. To understand the tradeoff between the number of iterations and signal and noise, Figure 8 demonstrates tradeoffs between number of iterations N with signal and noise, including similar scores for DIB and AVE (rSIR for $N = 1$) images. As the number of iterations is increased, the images sharpen and details become more evident (i.e. signal rms error decreases). However, the noise level also increases with increasing iterations. Thus, while the iteration improves the signal, excessive iteration can overly enhance the noise. Noting that we can stop the rSIR iteration at any point, we somewhat arbitrarily choose number of iterations N in the range $15-25$, trading off good signal performance with only slightly degraded the noise performance. The number of iterations, which varies by sensor and channel, is recorded in each file, in the `TB` variable-level attribute, `sir_number_of_iterations`.

6.5   rSIR Effective Resolution

Using the method described in Long et al. (2023), we evaluate the effective resolution of CETB image products using subsets over observed coastline and island crossings. In general, the extent of the spatial response function of a pixel in a remote sensing image can be larger than the pixel spacing (the posting resolution), so the effective extent of the pixels actually overlaps. This means that the effective resolution of the image is coarser than the posting resolution, which can be described as oversampled. Oversampled images can be resampled to coarser posting resolutions with limited loss of information. We have deliberately oversampled the posting resolution of CETB rSIR images, to allow users maximum flexibility in resampling options.

Similarly, we evaluate the effective linear resolution of CETB brightness temperatures (Long et al., 2021). For each sensor, channel and pass direction, we select multiple daily CETB fields for small (200 km x 200 km) Arctic regions with observations of both cold ocean and warm land surfaces (Figure 9). Two transects of ocean/land discontinuities, denoted as "coastline-crossing" and "island-crossing" cases, are analysed with GRD and rSIR images (Figure 10) to derive pixel spatial response functions (PSRFs). The derived PSRFs are compared to discrete step-model coast-land boundaries and to idealized Gaussian response functions. The effective resolution of the images is defined as the 3-dB width of the derived PSRFs (Figure 11).

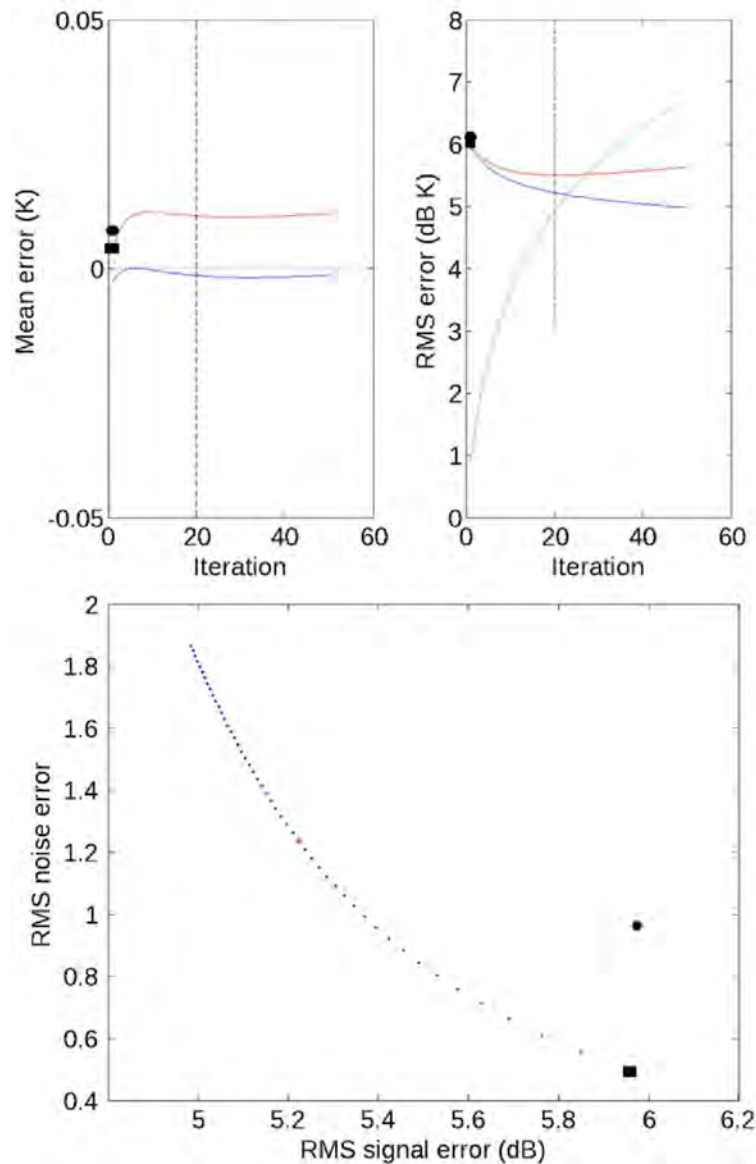As expected, the effective resolution of observed GRD PSRFs is coarser than that of the

Figure 8: *rSIR performance with increasing iterations. Mean error (upper left) and RMSE (upper right), for noisy (red line) vs. noise-free (blue line) measurements. Green line is noise power computed from the difference between noisy and noise-free cases, vertically displaced for clarity. The "optimum" (minimum error) number of iterations occurs at the bottom of the red curve. (Bottom) RMS noise power vs. RMS signal error by iteration, with increasing iterations from right to left. In each image, GRD (large circle), AVE (rSIR for $N = 1$) (large square) are denoted. rSIR for $N = 20$ (red star) is denoted in bottom plot (Long and Brodzik, 2016).*
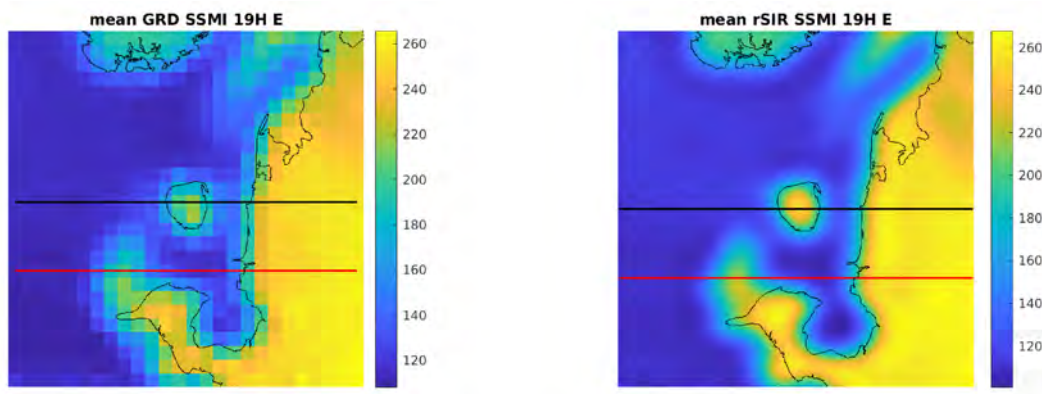
Figure 9: *Study area near Ostrov Kolguyev (Arctic Ocean, approximately 69N, 49E). Average of example daily SSM/I 19H T_B images, 2015 day of year 100-103, evening passes, from 25 km GRD (left) and 3.125 km rSIR, horizontal lines indicate locations of "island-crossing" (black) and "coastline-crossing" cases (Long et al., 2021).*
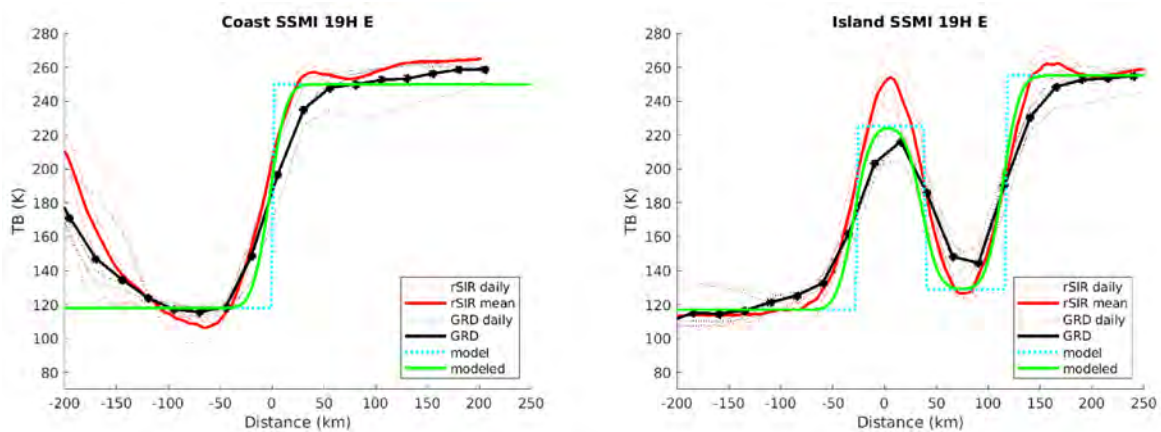

Figure 10: *Plots of T_B coast-crossing (left) and island-crossing (right) transects, for GRD, rSIR and modelled cases (Long et al., 2021).*

observed rSIR PSRFs. The effective linear resolution of rSIR images is demonstrated to be approximate 30% better than that of GRD images. Long et al. (2021) contains a comprehensive application of this methodology to the complete set of CETB sensors and channels, including an extensive Appendix with resolution comparisons for CETB SMMR, AMSR-E, SSM/I and SSMIS sensors. In practice, resolution enhancement depends on geolocation accuracy, geometry of available overlapping measurements and frequency sensitivity to rapid atmospheric and surface variability during the temporal period of observations.

6.6 Local-Time-of-Day

All of the CETB passive microwave sensors fly on near-polar, sun-synchronous satellites, which maintain an orbit plane with an orientation that is (approximately) fixed with respect to the sun. Thus the satellite crosses the equator on its ascending (northbound) path at the same local time of day (within a small tolerance). The resulting coverage pattern yields passes about 12 hours apart in local-time-of-day (ltod) at the equator. Most areas near the pole are covered multiple times per day. Analyzing the data from a single sensor, we find that polar measurements fall into two ltod ranges. The two periods are typically less than 4 hours long, and are spaced 8 or 12 hours apart. Significantly, due to the orbit repeat cycle, two succeeding days at any particular location may make measurements at different ltod, and therefore different times during the diurnal cycle (Gunn, 2007). When not properly accounted for, this introduces undesired variability (noise) into a time series analysis.

Heritage gridded T_B products have either (1) selected measurements from only one pass over the day or (2) averaged all measurements during the day into a given grid cell. Microwave brightness temperature is defined as the product of surface physical temperature and surface emissivity. Since surface temperatures can fluctuate widely during the day, the latter is not generally useful, effectively smearing diurnal temperature fluctuations in the averaged T_B. The former discards large amounts of potentially useful data. Some heritage products split images into "ascending pass-only" and "descending pass-only" data, resulting in two images per day. This is a reasonable approach at low latitudes, but at higher latitudes, the ascending/descending division does not work as well, since adjacent pixels along swath overlap edges can come from widely different ltod (which vary on subsequent days). The gridded T_B image, ostensibly representing consistent local times of day, actually represented different physical temperature conditions.

Another alternative is to split the data into two images per day based on the ltod approach of Gunn and Long (2008). We consider separating measurements in a coverage swath by local time-of-day (ltod) compared to ascending/descending. The essential idea is to keep measurements with similar local time of day together. As illustrated in Figure 12, as a swath passes near the North Pole, the orbit direction changes from ascending (northbound) to descending (south-bound). This occurs at the point when the ground track of the spacecraft nadir achieves its northernmost extent. In other words, the spacecraft nadir
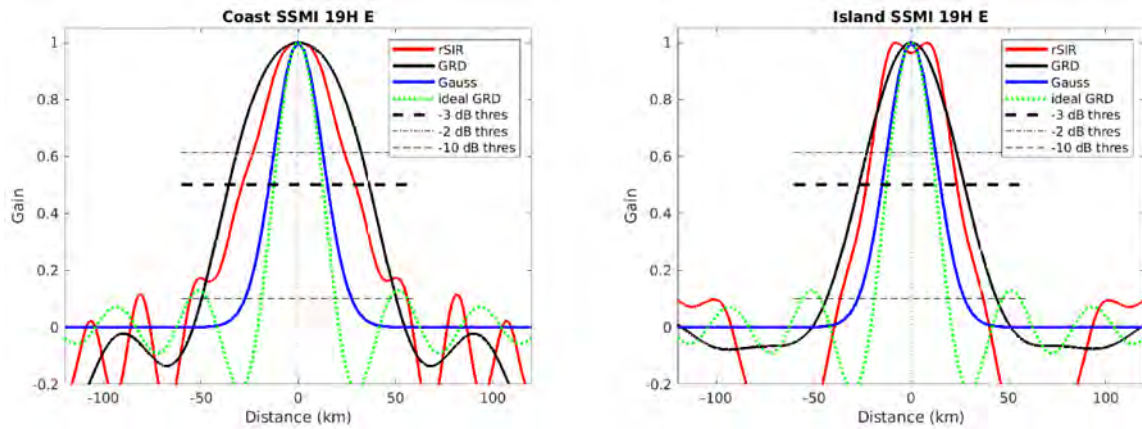
Figure 11: *Derived single-pass rSIR and GRD PSRFs from coast-crossing (left) and island-crossing (right) transects, compared with modelled (Gaussian and ideal step-function) cases. Width of PSRF at 3-dB threshold is interpreted as effective resolution (Long et al., 2021).*
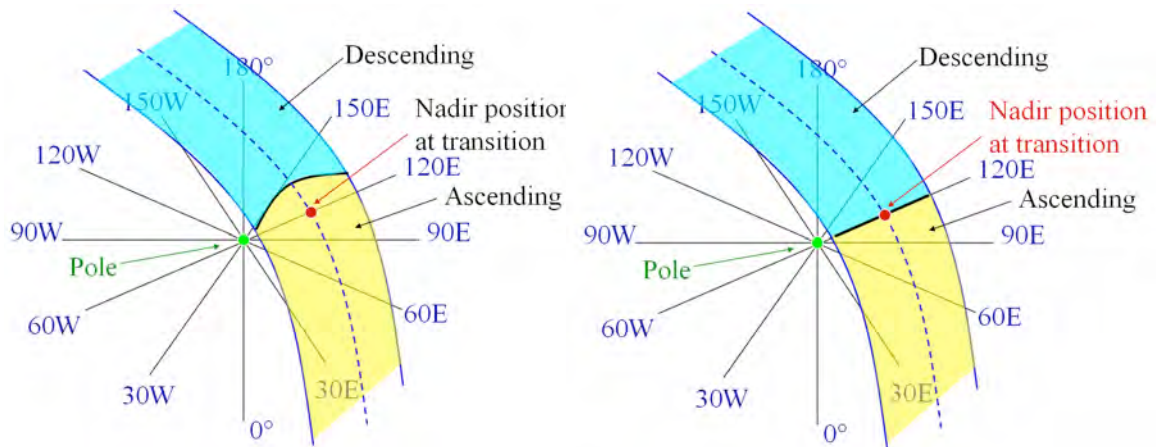

Figure 12: *Illustration of the boundaries in the areal coverage between (left) ascending/descending division and (right) local time-of-day division of measurements in a single orbit pass over the Northern Hemisphere.*

location is used to divide the data into ascending and descending regions. In the ascending/descending division, all data collected before this point is considered "ascending" data, and data collected afterward is considered "descending." Since the antenna is rotating and looking outward, data classified as "ascending" can actually be along the descending portion of the swath.

In contrast, in ltod division, the local time of day is computed as the UTC time in minutes plus 4 times the longitude in degrees ($\pm 180.0°$). Data that are collected before the ltod division point (which in Figure 12 corresponds to $120°$E) is assigned to the "ascending" data group, while data collected after this time (in ltod) is assigned as "descending" data. Note the division line occurs along a fixed line of longitude. In practice the division line does not have to pass through the nadir position of the transition of the spacecraft from ascending to descending.

Since the radiometer is in a sun-synchronous orbit, a given point of the Earth's surface is observed at the same ltod for each pass in the orbit repeat cycle. To illustrate this, consider a 1-degree wide latitude band, $70°$–$71°$, in the Northern or Southern hemisphere. Note that within a given latitude band, all the measurements fall within one of two narrow ltod periods. The precise value (in ltod) of the band depends on the orbit and is different for different sensors (see Appendix E for details).

Except at the highest latitudes, the measurements collected from a given sensor can be naturally grouped into two different ltod groups. If we repeated the analysis at the equator the two ltod groups would correspond to ascending and descending passes. At the poles, however, the ascending/descending division does not do a good job of properly dividing the data into its natural groups. For the azimuthal grids, we therefore divide measurement data by ltod, rather than using the spacecraft ascending/descending flag.

We note that heritage products that included daily average images would have included all data regardless of ltod, and thus in the polar regions, would have combined data observed many hours apart. The ltod division ensures that even if data are combined from different passes, the data fall within the natural ltod data grouping. Using the natural ltod data divisions, two images per day can be generated. Unlike daily or ascending/descending division, all measurements averaged into a single pixel come from the same narrow ltod grouping, which minimizes artifacts that may have otherwise introduced from rapidly changing conditions on the surface.

One drawback to using an ltod division scheme is that in a polar image there is a longitude line in the image that divides data from the previous and current day. Temporal changes at the surface can produce discontinuities across this line. In most cases, the satellite orbit was stable enough to allow a fixed ltod division time for the sensor lifetime; however, in some cases orbital drift was significant and justified changes in the ltod settings, to ensure that the twice-daily temporal divisions were capturing the intended groups of local times in the respective files. See Appendix E for plots summarizing this analysis, by sensor and (where necessary) year.

7   CETB Product Description

7.1   Product Description

The CETBv2 data product consists of Level 3 gridded, twice-daily, calibrated radiometric brightness temperature data for each polarization channel (H and V) on the EASE-Grid 2.0 Azimuthal and Cylindrical projections. CETB processing includes both low-noise (low-resolution) gridded data and enhanced-resolution data grids, with potentially higher noise, to enable product users to compare and choose which option better suits a particular research application.

All radiometer channels are gridded to the coarsest resolution (25 km) grids using the GRD drop-in-the-bucket method described in Section 6.2. This produces gridded data with the smoothest, lowest noise possible, at the expense of resolution. All channels are also gridded using the rSIR image reconstruction method (Section 6.3), at enhanced resolutions on nested grids at power-of-2 divisors of the base 25 km grid (Figure 2). The enhanced resolution chosen for each frequency depends on spatial field of view (Table 16). Figure 13 describes generalized system architecture.

7.2   Passive Microwave Sensors

Radiometer data from the following sensors are included in CETBv2: Nimbus-7 SMMR; DMSP-F08, -F10, -F11, -F13, -F14, -F15 SSM/I; DMSP-F16, -F17, -F18 and -F19 SSMIS; Aqua AMSR-E; and GCOMW1 AMSR2.

7.3   Temporal Coverage

Twice-daily grids are produced, by local time of day passes, over the useful life of each sensor (see Section 6.6 for details on local time of day separation). This ensures that all measurements in any one image have consistent spatial/temporal relationships while retaining as much data as possible. The CETB adopts the ltod division scheme for the Northern and Southern hemispheres. In the equatorial region for the EASE2-T grids, ltod is equivalent to splitting by ascending vs. descending passes. Each file includes a temporal grid with time averages of the measurements combined into each pixel. This enables investigators to explicitly account for the ltod temporal variation of the measurements included in a particular pixel. To account for the differences in orbits of the different sensors, the ltod division for the twice-daily images varies between sensors and (if there was orbital drift), possibly with time. See Appendix E for sensor ltod values.
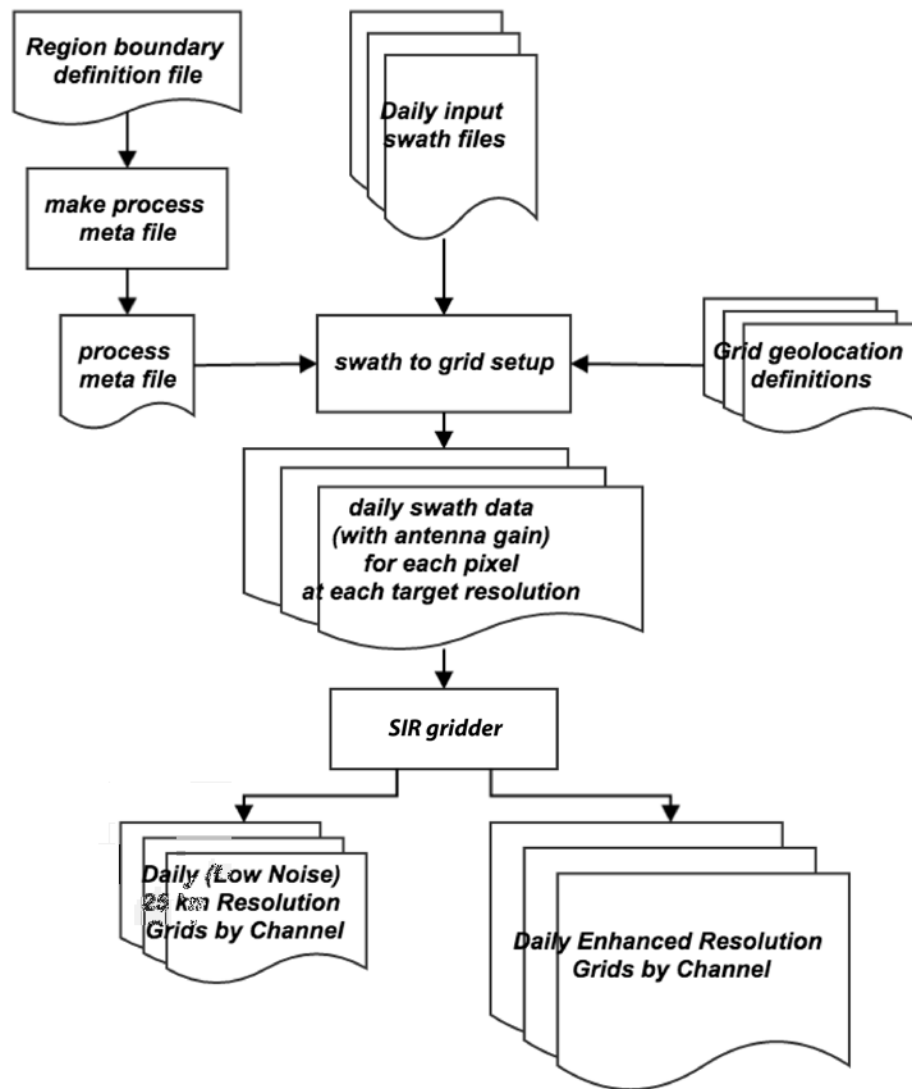
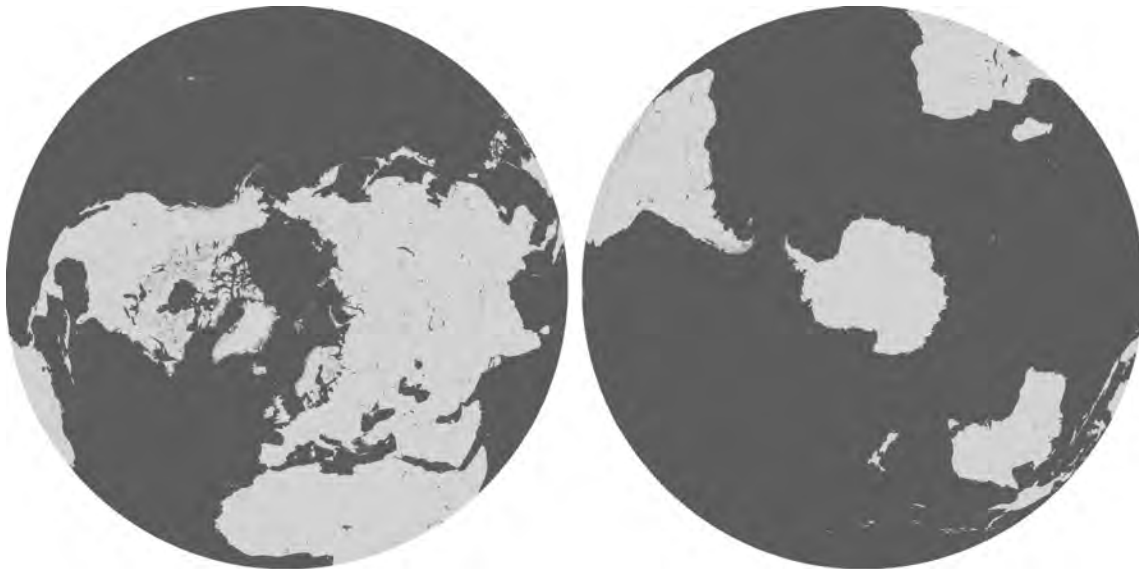**Figure 13:** *CETB system architecture.*

Figure 14: *Northern and Southern EASE-Grid 2.0 projection extents. Land-ocean mask from Brodzik and Knowles (2011).*

7.4   Spatial Extent

Azimuthal grids extend to the full Northern (EASE2-N, EPSG:6931) and Southern (EASE2-S, EPSG:6932) hemispheres, respectively, as described in Brodzik et al. (2012, 2014) (Figure 14). Equal-area cylindrical projections suffer increasing aspect distortion as grid cells approach the poles. For this reason, and to reduce computation time and storage requirements for the CETB product, the cylindrical Temperate and Tropical (EASE2-T, EPSG:6933) grid is limited to latitudes equatorward of +/-67.1 degrees (Figure 15). The EASE2-T 25 km projection is a subset of the standard EASE-Grid 2.0 25 km global projection (EASE2-M), with the upper left corner of the EASE2-T grids extent exactly aligned to the upper left corner of the EASE2-M 25 km grid cell at column 0, row 22. The upper left corner grid cell is defined to be column 0, row 0 (Figure 16). See Appendix B for grid specifications.

7.5   Grid Spatial Resolution

The coarsest grid resolution is 25 km, with enhanced-resolution grids defined in a nested fashion (Figure 17 and Appendix B), in powers of 2, at 12.5, 6.25 and 3.125, according to Brodzik et al. (2012, 2014). The effective resolution enhancement for rSIR CETB images is 30–60% finer than conventionally processed gridded data (Long, 2021).

Figure 15: *Cylindrical EASE-Grid 2.0 projection extents. Full extent coverage is EASE2-M, with horizontal red lines delineating the smaller latitudinal extent of EASE2-T grid used for CETBv2 product. Land-ocean mask from Brodzik and Knowles (2011).*

7.6 Radiometer Channels and Grid Resolution

We define a radiometer channel as a particular frequency and polarization combination. Separate images are generated for each sensor and radiometer channel. Data from different sensors are not combined in the same images. All channels are processed as both conventional and enhanced-resolution products. Conventional resolution is defined to be $25\,\mathrm{km}$; actual resolution enhancement is dependent on frequency (more details in Appendix C.3). Table 6 summarizes the CETB channels for each sensor.

Table 6: *CETBv2 sensors and channels. (SSMIS 150-182 GHz channels are not included in the CETB.)*

Sensor	Channels
SMMR	6.6H, 6.6V, 10.7H, 10.7V, 18H, 18V, 21H, 21V, 37H, 37V
SSM/I	19H, 19V, 22V, 37H, 37V, 85H, 85V
SSMIS	19H, 19V, 22V, 37H, 37V, 91H, 91V
AMSR-E	6.9H, 6.9V, 10.7H, 10.7V, 18.7H, 18.7V, 23.8H, 23.8V, 36.5H, 36.5V, 89.0H, 89.0V
AMSR2	6.9H, 6.9V, 10.7H, 10.7V, 18.7H, 18.7V, 23.8H, 23.8V, 36.5H, 36.5V, 89.0H, 89.0V

Projection/grid relationship of EASE2_M25km to EASE2_T25km
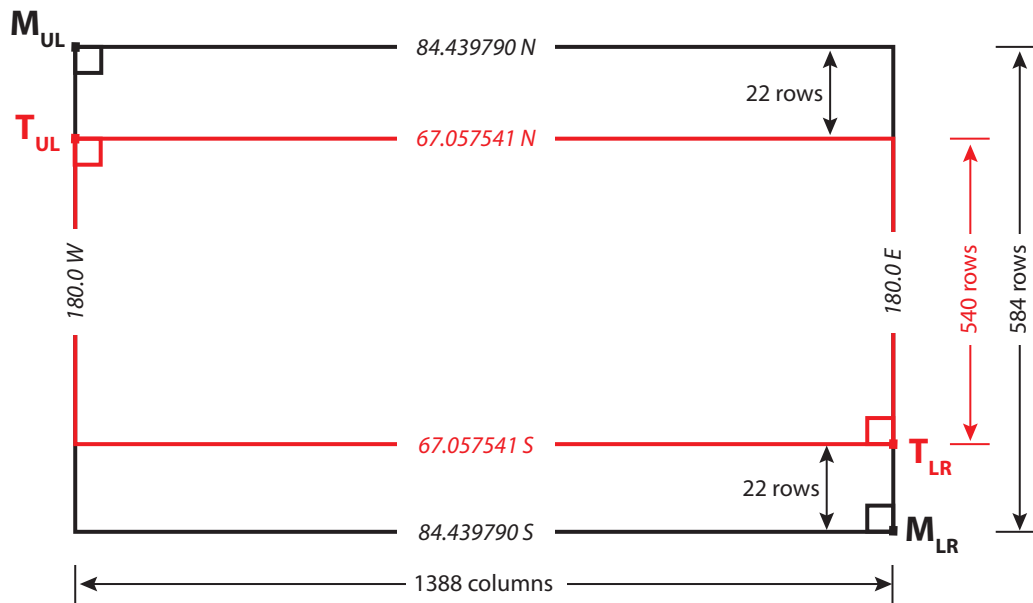
Location	Description	EASE2_M25 Grid Coordinates (col, row)	EASE2_T25 Grid Coordinates (col, row)
MUL	EASE2_M25km outer corner of upper left cell	(-0.5, -0.5)	n/a
TUL	EASE2_T25km outer corner of upper left cell	(-0.5, 21.5)	(-0.5, -0.5)
TLR	EASE2_T25km outer corner of lower right cell	(1387.5, 561.5)	(1387.5, 537.5)
MLR	EASE2_M25km outer corner of lower right cell	(1387.5, 583.5)	n/a

Figure 16: *Relationship of CETB EASE2-T projection to global EASE2-M coverage, for respective 25 km grids. (Difference in latitudinal extent is exaggerated, see Figure 15 for actual difference in projected area.) (Brodzik et al., 2016).*
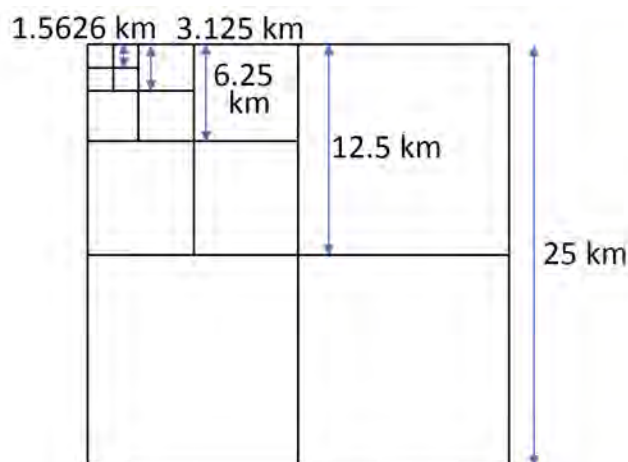
Figure 17: *Nested relationships of azimuthal 25 km base resolution cells. Actual values of cylindrical cell sizes are slightly different, but nesting relationships are analagous.*

7.7 File Contents

CETBv2 products are distributed as NetCDF files, using the Climate and Forecast (CF) Metadata Conventions v1.9 for product and file metadata. Appendix D contains filename and metadata content. CETB brightness temperature files contain one brightness temperature array variable per file, with additional ancillary variables, including local time-of-day (ltod), measurement count, brightness temperature standard deviation and average incidence angle of contributing measurements.

   File-level metadata includes the list of input swath files used, SIR iteration parameters, projection definitions, and provenance metadata to identify the source and processing version used to produce the data contents. For all channels, estimated brightness temperature accuracy is better than 0.5 K worst-case over the entire data set. No correction for atmospheric effects is applied.

   Each CETB file contains 1-dimensional coordinate variables with time, x and y, containing projected locations at the center of each pixel, in meters from the origin of the projection. The file also contains a coordinate reference system (crs) variable with CF-compliant description of the projected data, along with other popular descriptions, including proj.4 strings and EPSG codes used automatically by many popular geolocation packages, including GDAL.

   For each CETB projection and grid resolution, an ancillary data file is produced, with geolocation latitude and longitude at the center of each grid cell. Latitude and longitude are determined by projection and grid resolution. Since there is nothing CETB-project specific about these geolocation files, they are released as an ancillary data set, for use by anyone needing this information for these EASE-Grid 2.0 projections/grids. The geolocation data

are distributed seperately, by projection and grid (Stewart et al., 2022).

The following images include sample GRD (25 km) and rSIR (3.125 km) brightness temperatures for the Northern (EASE2-N), Southern (EASE2-S) and cylindrical Temperate and Tropical (EASE2-T) projections for AMSR2 channel 36H T_Bs for 30 Apr 2023.

NSIDC0630_GRD_EASE2_N25km_GCOMW1_AMSR2_M_36H_20230430_v2.0.nc
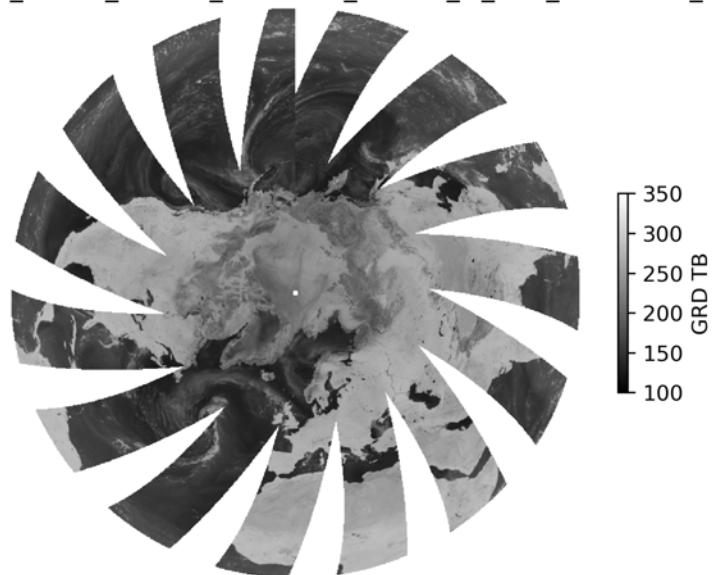
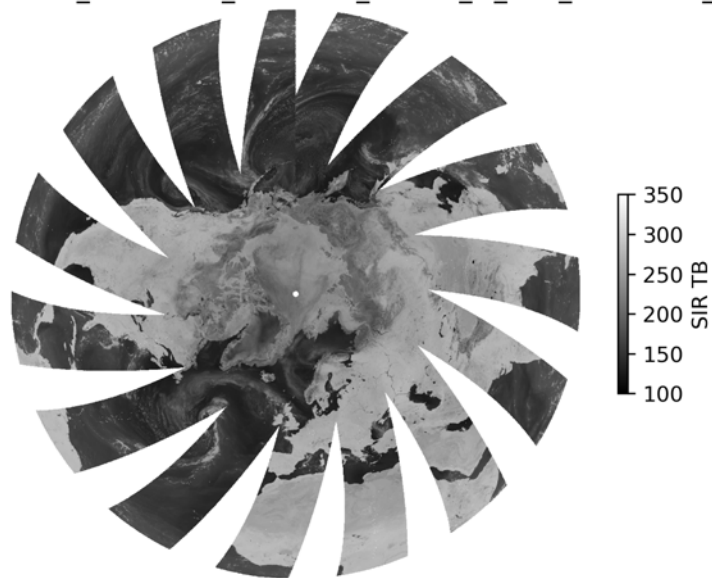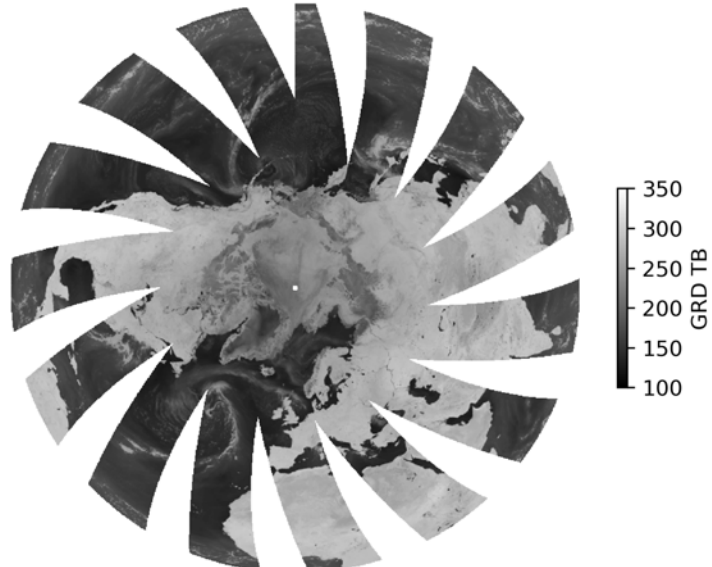NSIDC0630_SIR_EASE2_N3.125km_GCOMW1_AMSR2_M_36H_20230430_v2.0.nc

Figure 18: *CETBv2 Northern Hemisphere AMSR2 morning ltod pass 36H GRD 25 km (top) and rSIR 3.125 km (bottom) brightness temperatures, 30 Apr 2023.*

NSIDC0630_GRD_EASE2_N25km_GCOMW1_AMSR2_E_36H_20230430_v2.0.nc

NSIDC0630_SIR_EASE2_N3.125km_GCOMW1_AMSR2_E_36H_20230430_v2.0.nc

Figure 19: *CETBv2 Northern Hemisphere AMSR2 evening ltod pass 36H GRD 25 km (top) and rSIR 3.125 km (bottom) brightness temperatures, 30 Apr 2023.*

Figure 20: *CETBv2 Southern Hemisphere AMSR2 morning ltod pass 36H GRD 25 km (top) and rSIR 3.125 km (bottom) brightness temperatures, 30 Apr 2023.*

NSIDC0630_GRD_EASE2_S25km_GCOMW1_AMSR2_E_36H_20230430_v2.0.nc
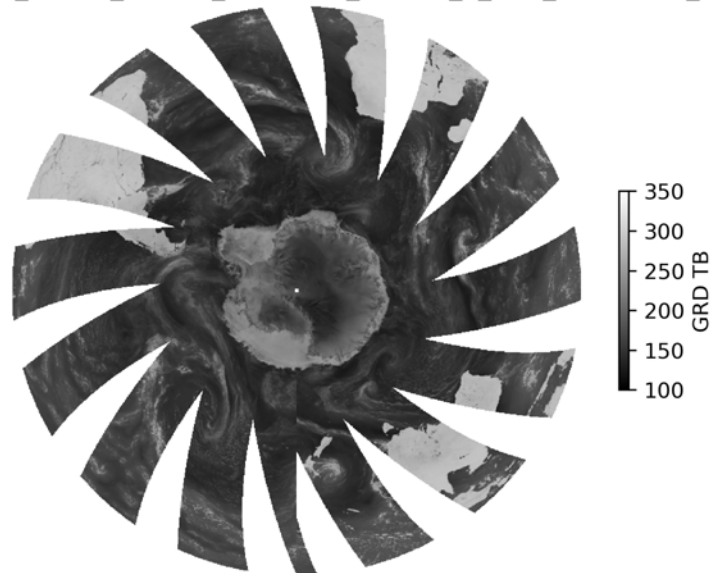
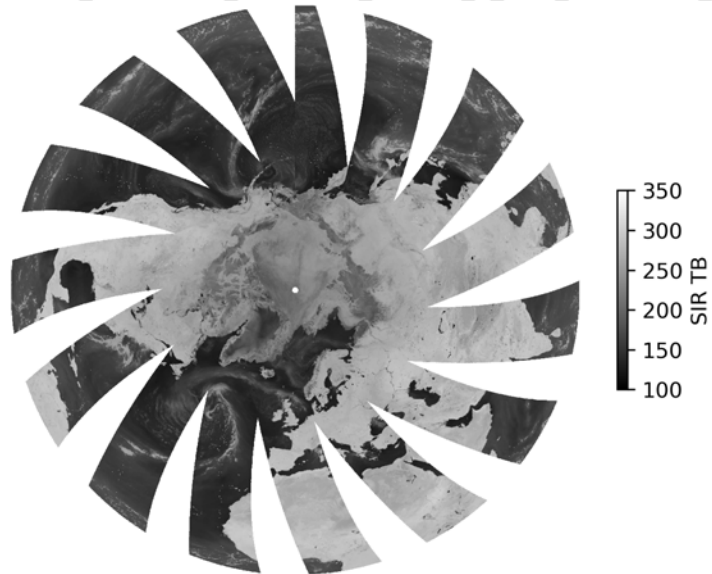NSIDC0630_SIR_EASE2_S3.125km_GCOMW1_AMSR2_E_36H_20230430_v2.0.nc
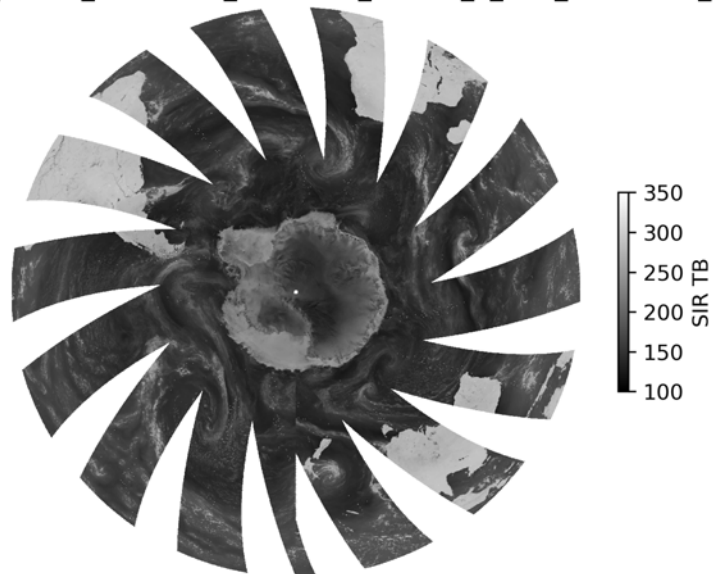
Figure 21: *CETBv2 Southern Hemisphere AMSR2 evening ltod pass 36H GRD 25 km (top) and rSIR 3.125 km (bottom) brightness temperatures, 30 Apr 2023.*

NSIDC0630_GRD_EASE2_T25km_GCOMW1_AMSR2_A_36H_20230430_v2.0.nc

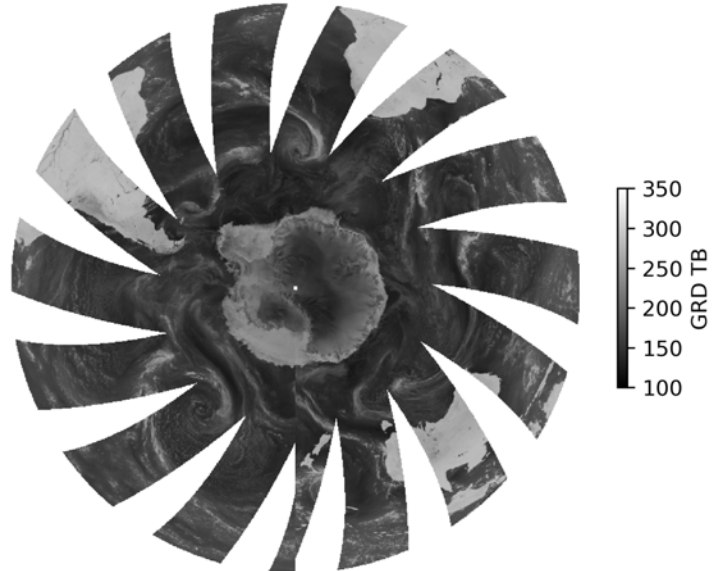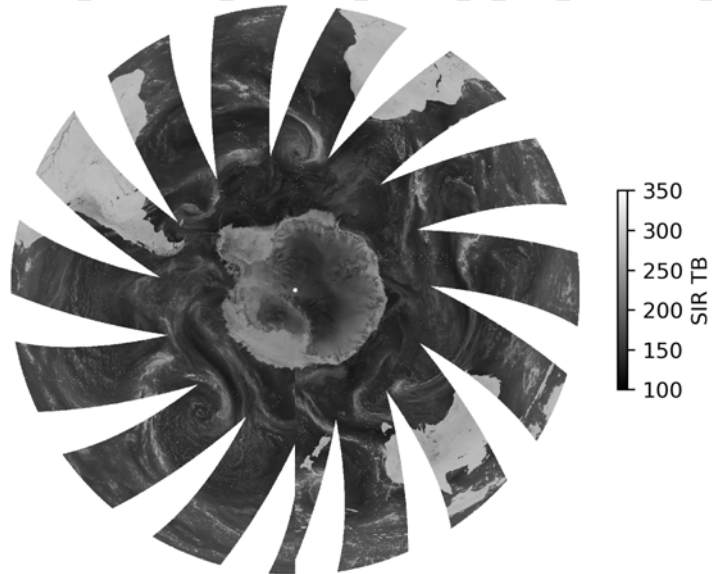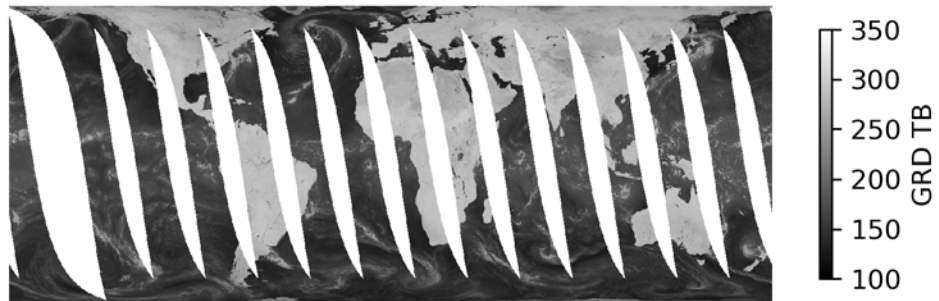NSIDC0630_SIR_EASE2_T3.125km_GCOMW1_AMSR2_A_36H_20230430_v2.0.nc

Figure 22: *CETBv2 Cylindrical AMSR2 ascending pass 36H GRD 25 km (top) and rSIR 3.125 km (bottom) brightness temperatures, 30 Apr 2023.*

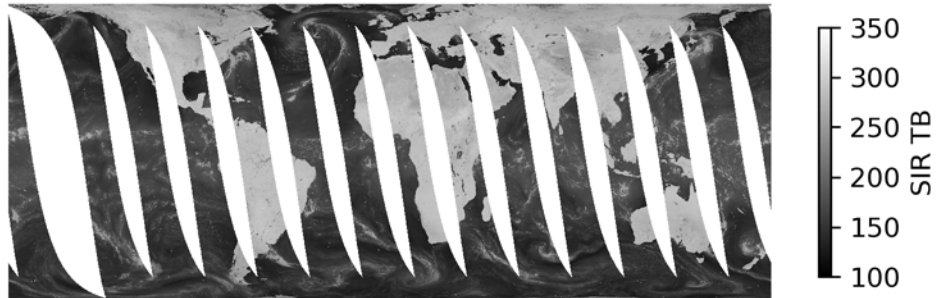**Figure 23:** *CETBv2 Cylindrical AMSR2 descending pass 36H GRD 25 km (top) and rSIR 3.125 km (bottom) brightness temperatures, 30 Apr 2023.*

7.8 Data Volume

Assuming negligible size of file-level metadata relative to variable contents, uncompressed CETB data volume can be estimated as follows.

7.8.1 GRD Data Volume

For a total size on SSM/I low res file volume of 224 MB/day (about 82 GB/year/sensor)

Table 7: *CETB file data elements*

Layer	Element Size
TB	2-byte unsigned int
TB_time	2-byte signed int
TB_std_dev	2-byte unsigned int
TB_num_samples	1-byte unsigned int
Incidence_angle	2-byte signed int

Table 8: *GRD daily file volume per channel per pass direction, by projection*

Grid	Columns	Rows	Element Size (bytes)	Uncompressed File Volume (bytes)[1]
EASE2-N25km	720	720	9	4,665,600
EASE2-S25km	720	720	9	4,665,600
EASE2-T25km	1388	540	9	6,745,680
Total bytes per grid set				16,076,880

GRD files are produced for 2 passes per day per channel. Maximum volume for GRD files is: 2 passes/day * N channels * 16 MB per set = 32 MB/day/channel * N channels/radiometer. For the 7-channel SSM/I radiometers, GRD maximum file volume is 224 MB/day, (82 GB/year). Actual file volume depends on compression.

Table 9: *rSIR daily file volume per channel per pass direction, by projection*

Grid	Columns	Rows	Element Size (bytes)	Uncompressed File Volume (bytes)[1]
EASE2-N/S12.5km	1440	1440	9	18,662,400
EASE2-T6.25km	2776	1080	9	26,982,720
Total bytes per 12.5 km set				45,645,120
EASE2-N/S6.25km	2880	2880	9	74,649,600
EASE2-T6.25km	5552	2160	9	107,930,880
Total bytes per 6.25 km set				182,580,480
EASE2-N/S3.125km	5760	5760	9	298,598,400
EASE2-T3.125km	11104	4320	9	431,723,520
Total bytes per 3.125 km set				730,321,920

7.8.2   rSIR Data Volume

GRD files are produced for 2 passes per day per channel at 25 km. rSIR files are produced for 2 passes per day per channel at one of 12.5 km, 6.25 km or 3.125 km, depending on frequency. GRD and rSIR data elements included in a give file are the same (Table 7), with small differences in variable metadata. Daily compressed file sizes depend on sensor swath size and available input coverage on a given day, varying from 4-106 MB/file/day. A data day from a typical SSM/I file set ranges from 230 MB to 11 GB with an average size of 5 GB/day. A typical user is expected to require data from only one of the three projections, therefore, data volume will depend on user requirements for spatial and temporal coverage, as well as frequencies and gridding method.

The total compressed volume of the CETBv2 data through end of 2022, including SMMR, AMSR-E, AMSR2, six SSM/Is, four SSMISs, is 65 TB, in approximately 14 million granules.

8 Acknowledgements

8.1 Funding Resources

8.2 Supercomputing Resources

8.3 Software

Software to produce the CETB product includes `gsx`, the eXtended Generic Swath translator that converts various passive microwave swath brightness temperature products into a generic netCDF format. This provides a common data representation of passive microwave swath data such that downstream processing can be written against the GSX netCDF contents. Complex source data differences are encapsulated in the GSX files. The `gsx` software is licensed under the GNU General Public License v3.0, available at: `https://github.org/nsidc/gsx`. This repository is currently private, but is scheduled to be made public in 2023.

Software to process extended generic swath files into GRD and/or rSIR images is licensed under the GNU General Public License v3.0, available at: `https://github.org/nsidc/pmesdr`. This repository is currently private, but is scheduled to be made public in 2023.

References

Backus, G. E. and J. F. Gilbert. 1967. Numerical Applications of a Formalism for Geophysical Inverse Problems. *Geophysical Journal International 13*(1-3), 247–276. doi:https://doi.org/10.1111/j.1365-246X.1967.tb02159.x.

Beitsch, A., L. Kaleschke, and S. Kern. 2014. Investigating High-Resolution AMSR2 Sea Ice Concentrations during the February 2013 Fracture Event in the Beaufort Sea. *Remote Sensing 6*(5), 3841–3856. doi:https://doi.org/10.3390/rs6053841.

Berg, W., R. Kroodsma, C. D. Kummerow, and D. S. McKague. 2018. Fundamental Climate Data Records of Microwave Brightness Temperatures. *Remote Sensing 10*(8), 1306. doi:https://doi.org/10.3390/rs10081306.

Brodzik, M. J., B. Billingsley, T. Haran, B. Raup, and M. H. Savoie. 2012. EASE-Grid 2.0: Incremental but Significant Improvements for Earth-Gridded Data Sets. *ISPRS Int. J. Geo-Inf. 1*, 32–45. doi:https://doi.org/10.3390/ijgi1010032.

Brodzik, M. J., B. Billingsley, T. Haran, B. Raup, and M. H. Savoie. 2014. Correction: Brodzik, M.J., *et al.* EASE-Grid 2.0: Incremental but Significant Improvements for Earth-Gridded Data Sets, *ISPRS Int. J. Geo-Inf.* 2012, 1, 32–45. *ISPRS Int. J. Geo-Inf. 3*, 1154–1156. doi:https://doi.org/10.3390/ijgi3031154.

Brodzik, M. J. and K. Knowles. 2011. EASE-Grid 2.0 Land-Ocean-Coastline-Ice Masks Derived from Boston University MODIS/Terra Land Cover Data. NASA National Snow and Ice Data Center DAAC, Boulder, CO USA. Digital Media, http://nsidc.org/data/nsidc-0610, doi:https://doi.org/10.5067/XR8523MC24TB.

Brodzik, M. J. and D. G. Long. 2018, April. Calibrated Passive Microwave Daily EASE-Grid 2.0 Brightness Temperature ESDR (CETB) Algorithm Theoretical Basis Document, version 1.0. doi:https://doi.org/10.5281/zenodo.7958456.

Brodzik, M. J., D. G. Long, and M. A. Hardman. 2018. Best Practices in Crafting the Calibrated, Enhanced–Resolution Passive–Microwave EASE-Grid 2.0 Brightness Temperature Earth System Data Record. *Remote Sensing 10*(11). doi:https://doi.org/10.3390/rs10111793.

Brodzik, M. J., D. G. Long, and M. A. Hardman. 2021. SMAP Radiometer Twice–Daily rSIR–Enhanced EASE-Grid 2.0 Brightness Temperatures, Version 2.0. NASA National Snow and Ice Data Center DAAC, Boulder, CO USA. Digital Media, http://nsidc.org/data/nsidc-0738, updated daily, doi:https://doi.org/10.5067/YAMX52BXFL10.

Brodzik, M. J., D. G. Long, and M. A. Hardman. 2023. Calibrated Enhanced-Resolution Passive Microwave Daily EASE-Grid 2.0 Brightness Temperature ESDR, Version 2. National Snow and Ice Data Center Distributed Active Archive Center, Boulder, CO USA. Digital Media, `https://nsidc.org/data/nsidc-0630/versions/2`, updated daily, doi:`https://doi.org/10.5067/19LHYLUXZ22M`.

Brodzik, M. J., D. G. Long, M. A. Hardman, A. Paget, and R. L. Armstrong. 2016. MEaSUREs Calibrated Enhanced-Resolution Passive Microwave Daily EASE-Grid 2.0 Brightness Temperature ESDR, Version 1. National Snow and Ice Data Center, Boulder, CO USA. Digital Media, `http://nsidc.org/data/nsidc-0630/versions/1`, doi:`https://doi.org/10.5067/MEASURES/CRYOSPHERE/NSIDC-0630.001`.

Early, D. S. and D. G. Long. 2001, Feb. Image reconstruction and enhanced resolution imaging from irregular samples. *IEEE Transactions on Geoscience and Remote Sensing 39*(2), 291–302. doi:`https://doi.org/10.1109/36.905237`.

Eaton, B., J. Gregory, B. Drach, K. Taylor, S. Hankin, J. Blower, J. Caron, et al.. 2021. NetCDF Climate and Forecast (CF) Metadata Conventions, v1.9. Accessed 2023–06–14 at `http://cfconventions.org/Data/cf-conventions-1.9/cf-conventions.html`.

Eaton, B., J. Gregory, B. Drach, K. Taylor, S. Hankin, J. Caron, R. Signell, et al.. 2011. NetCDF Climate and Forecast (CF) Metadata Conventions, v1.6. Accessed 2018–08–02 at `http://cfconventions.org/cf-conventions/v1.6.0/cf-conventions.html`.

Gaiser, P. W., K. M. S. Germain, E. M. Twarog, G. A. Poe, W. W. Purdy, E. Richardson, W. Grossman, W. L. Jones, D. Spencer, G. Golba, J. Cleveland, L. Choy, R. M. Bevilacqua, and P. S. Chang. 2004. The WindSat Spaceborne Polarimetric Microwave Radiometer: Sensor Description and Early Orbit Performance. *IEEE Transactions on Geoscience and Remote Sensing 42*(11), 2347–2361. doi:`https://doi.org/10.1109/TGRS.2004.836867`.

Gloersen, P. and F. Barath. 1977. A Scanning Multichannel Microwave Radiometer for Nimbus-G and SeaSat-A. *IEEE Journal of Oceanic Engineering 2*(2), 172–178. doi:`https://doi.org/10.1109/JOE.1977.1145331`.

Gröchenig, K.. 1992. Reconstruction Algorithms in Irregular Sampling. *Math. Comp. 59*(1992), 181—194. doi:`https://doi.org/10.1090/S0025-5718-1992-1134729-0`.

Gunn, B.. 2007. Temporal Resolution Enhancement for AMSR Images. BYU Internal Report MERS 07-002, Accessed 2023–04–30 at `https://www.mers.byu.edu/docs/reports/MERS0702.pdf`.

Gunn, B. A. and D. G. Long. 2008. Spatial resolution enhancement of amsr tb images based on measurement local time of day. In *IGARSS 2008 - 2008 IEEE International Geoscience and Remote Sensing Symposium,* Volume 5, pp. 33–36. doi:`https://doi.org/10.1109/IGARSS.2008.4780020`.

Hardman, M. A., M. J. Brodzik, D. G. Long, J. Z. Miller, J. M. Ramage, W. Meier, and S. Stewart. 2022. Continuous Improvements to Calibrated, Enhanced-Resolution Brightness Temperatures (CETBs) for Near Real-Time Cryospheric Applications. Poster presentation at AGU Fall Meeting, C12B-0573, Chicago, IL, 12-16 December, doi:`https://doi.org/10.5281/zenodo.7958812`.

Hollinger, J.. 1989. DMSP Special Sensor Microwave/Imager Calibration/Validation, Final Report, Volume 1. July.

Hollinger, J., R. Lo, G. Poe, R. Savage, and J. Peirce. 1987. Special Sensor Microwave/Imager User's Guide. 14 September.

Hollinger, J. P., J. L. Peirce, and G. A. Poe. 1990. SSM/I Instrument Evaluation. *IEEE Transactions on Geoscience and Remote Sensing 28*(5), 781–790. doi:`https://doi.org/10.1109/36.58964`.

Imaoka, K., M. Kachi, M. Kasahara, N. Ito, K. Nakagawa, and T. Oki. 2010. Instrument Performance and Calibration of AMSR-E and AMSR2. *International Archives of the Photogrammetry, Remote Sensing and Spatial Information Science 38*(8), 13–18.

Kawanishi, T., T. Sezai, Y. Ito, K. Imaoka, T. Takeshima, Y. Ishido, A. Shibata, M. Miura, H. Inahata, and R. R. W. Spencer. 2003. The Advanced Microwave Scanning Radiometer for the Earth Observing System (AMSR-E), NASDA's Contribution to the EOS for Global Energy and Water Cycle Studies. *IEEE Transactions on Geoscience and Remote Sensing 41*(2), 184–194. doi:`https://doi.org/10.1109/TGRS.2002.808331`.

Kunkee, D. B., G. A. Poe, D. J. Boucher, S. D. Swadley, Y. Hong, J. E. Wessel, and E. A.Uliana. 2008. Design and Evaluation of the First Special Sensor Microwave Imager/Sounder. *IEEE Transactions on Geoscience and Remote Sensing 46*(4), 863–883. doi:`https://doi.org/10.1109/TGRS.2008.917980`.

Long, D. G.. 2008. Microwave Sensors - Active and Passive. In M. W. Jackson, R. R. Jensen, and S. A. Morain (Eds.), *Manual of Remote Sensing, Volume 1: Earth Observing Platforms and Sensors* (4th ed.)., pp. 119. Bethesda, MD: American Society for Photogrammetry and Remote Sensing.

Long, D. G.. 2015, March. An Investigation of Antenna Patterns for the CETB. doi:`https://doi.org/10.5281/zenodo.7959217`.

Long, D. G.. 2021. A Comparison in the Effective Resolution of Enhanced Resolution SSMIS TB Images Created from CSU FCDR and GPM L1C Files. NSIDC Special Report 22. National Snow and Ice Data Center. Boulder, CO. Accessed 2023–05–22 at `https://nsidc.org/sites/nsidc.org/files/technical-references/NSIDC-Special-Report-22.pdf`.

Long, D. G. and M. J. Brodzik. 2016, May. Optimum Image Formation for Spaceborne Microwave Radiometer Products. *IEEE Transactions on Geoscience and Remote Sensing 54*(5), 2763–2779. doi:`https://doi.org/10.1109/TGRS.2015.2505677`.

Long, D. G., M. J. Brodzik, and M. A. Hardman. 2019. Enhanced–Resolution SMAP Brightness Temperature Image Products. *IEEE Transactions on Geoscience and Remote Sensing 57*(7), 4151–4163. doi:`https://doi.org/10.1109/TGRS.2018.2889427`.

Long, D. G., M. J. Brodzik, and M. A. Hardman. 2021. The Effective Resolution of CETB Image Products. NSIDC Special Report 21. National Snow and Ice Data Center. Boulder, CO. Accessed 2023–05–22 at `https://nsidc.org/sites/nsidc.org/files/technical-references/NSIDC-Special-Report-21.pdf`.

Long, D. G., M. J. Brodzik, and M. A. Hardman. 2023. Evaluating the Effective Resolution of Enhanced Resolution SMAP Brightness Temperature Image Products. *Frontiers in Remote Sensing 4*(1073765), 16. doi:`https://doi.org/10.3389/frsen.2023.1073765`.

Long, D. G. and D. L. Daum. 1998. Spatial resolution enhancement of SSM/I data. *IEEE Transactions on Geoscience and Remote Sensing 36*(2), 407–417. doi:`https://doi.org/10.1109/36.662726`.

Long, D. G. and M. R. Drinkwater. 2000. Azimuth Variation in Microwave Scatterometer and Radiometer Data over Antarctica. *IEEE Transactions on Geoscience and Remote Sensing 38*(4), 1857–1870. doi:`https://doi.org/10.1109/36.851769`.

Maeda, T., Y. Taniguchi, and K. Imaoka. 2016. GCOM–W1 AMSR2 Level 1R Product: Dataset of Brightness Temperature Modified Using the Antenna Pattern Matching Technique. *IEEE Transactions on Geoscience and Remote Sensing 54*(2), 770–782. doi:`https://doi.org/10.1109/TGRS.2015.2465170`.

Njoku, E., B. Rague, and K. Fleming. 1998. The Nimbus-7 SMMR Pathfinder Brightness Temperature Data Set. JPL Publication 98–4.

Njoku, E. G.. 2003. Nimbus–7 SMMR Pathfinder Brightness Temperatures, Version 1. NASA National Snow and Ice Data Center DAAC, Boulder, CO USA. Digital Media, `http://nsidc.org/data/nsidc-0036`, doi:`https://doi.org/10.5067/7Y1XWXT07HH8`.

Njoku, E. G., J. M. Stacey, and F. T. Barath. 1980. The Seasat Scanning Multichannel Microwave Radiometer (SMMR): Instrument Description and Performance. *IEEE Journal of Oceanic Engineering 5*(2), 100–115. doi:https://doi.org/10.1109/JOE.1980.1145458.

PPS, N.. 2023. Global Precipitation Measurement File Specification for GPM Products, Version 7.15 TKIO 3.100. Accessed 2023–05–11 at https://gpmweb2https.pps.eosdis.nasa.gov/pub/GPMfilespec/filespec.GPM.pdf.

Stephen, H. and D. G. Long. 2005. Modeling Microwave Emissions of Erg Surfaces in the Sahara Desert. *IEEE Transactions on Geoscience and Remote Sensing 43*(12), 2822–2830. doi:https://doi.org/10.1109/TGRS.2005.857899.

Stewart, J. S., M. J. Brodzik, and D. J. Scott. 2022. EASE Grids Ancillary Grid Information, Version 1. doi:https://doi.org/10.5067/GE8ET0MZ5ZVF.

Ulaby, F. T. and D. G. Long. 2014. *Microwave Radar and Radiometric Remote Sensing*. Ann Arbor, MI, USA: University of Michigan Press.

Wentz, F. J.. 1992. Measurement of Oceanic Wind Vector using Satellite Microwave Radiometers. *IEEE Transactions on Geoscience and Remote Sensing 30*(5), 960–972. doi:https://doi.org/10.1109/36.175331.

Appendices

A CETB Radiometers

A.1 SSM/I

The Special Sensor Microwave/Imager (SSM/I) is a total-power radiometer with seven operating channels, see Table 10. These channels include four frequencies with horizontal and vertical polarizations channels at 19.35, 37.0, and 85.5 GHz, and a vertical polarization channel at 22.235 GHz (Hollinger et al., 1990). An integrate-and-dump filter is used to make radiometric brightness temperature measurements as the antenna scans the ground track via antenna rotation (Hollinger, 1989). The 3 dB elliptical antenna footprints range from about 15-70 km in the cross-scan direction and 13-43 km in the along-scan direction depending on frequency (Hollinger et al., 1987). First launched in 1972, SSM/I instruments have flown on multiple spacecraft continuously until the present on the Defense Meteorological Satellite Program (DMSP) (F) satellite series.

Table 10: *SSM/I channel characteristics (Hollinger et al., 1990)*

Channel	Center Frequency (GHz)	Footprint (km)
19H	19.35	43 x 69
19V	19.35	43 x 69
22V	22.235	40 x 60
37H	37.0	29 x 37
37V	37.0	28 x 37
85H	85.5	13 x 15
85V	85.5	13 x 15

The SSM/I scanning concept is illustrated in Figure 24. The antenna spin rate is 31.6 rpm with an along-track spacing of approximately 12.5 km. The measurements were collected at a nominal incidence angle of approximately $53 \deg$. The scanning geometry produces a swath coverage diagram as shown in Figure 25. Figure 26 contains an illustration of antenna footprints on the surface for different antenna azimuth angles. The integrate and dump filters are 3.89 ms long for the 85 GHz channels and 7.95 ms long for the other channels. The time between samples is 4.22 ms long for the 85 GHz channels and 8.44 ms long for the other channels.
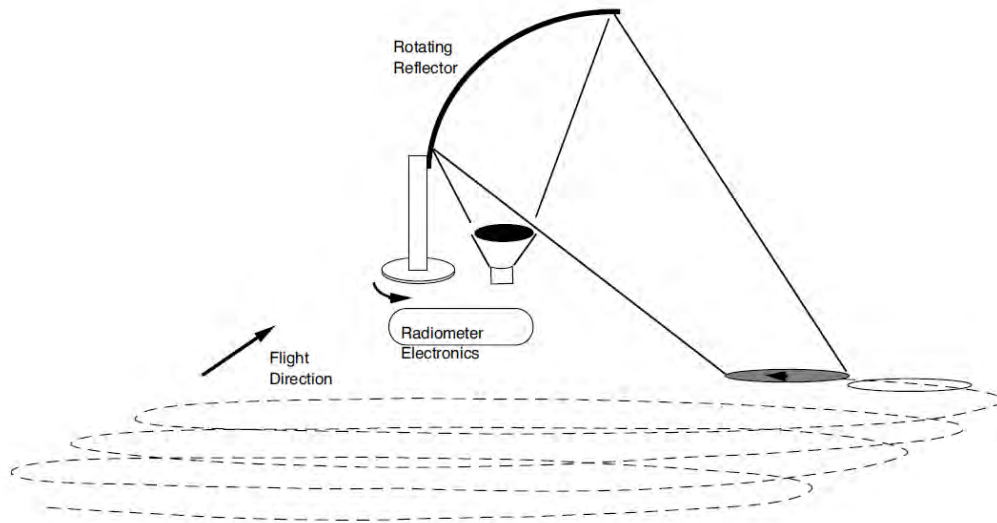
Figure 24: *Illustration of the SSM/I scanning concept. The antenna and feed are spun about the vertical axis. Only part of the rotation is used for measuring the surface T_B. The rest is used for calibration. The incidence angle is essentially constant as the antenna scans the surface (Long, 2008).*
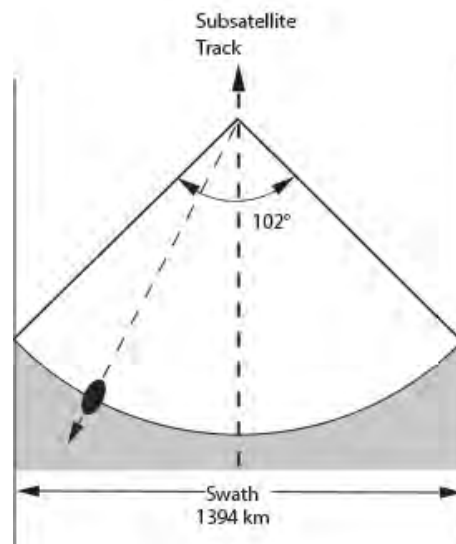
Figure 25: *SSM/I coverage swath. The dark ellipse schematically illustrates the antenna 3 dB response main lobe on the surface for a particular channel. The orientation of the ellipse varies as a function of antenna azimuth angle.*
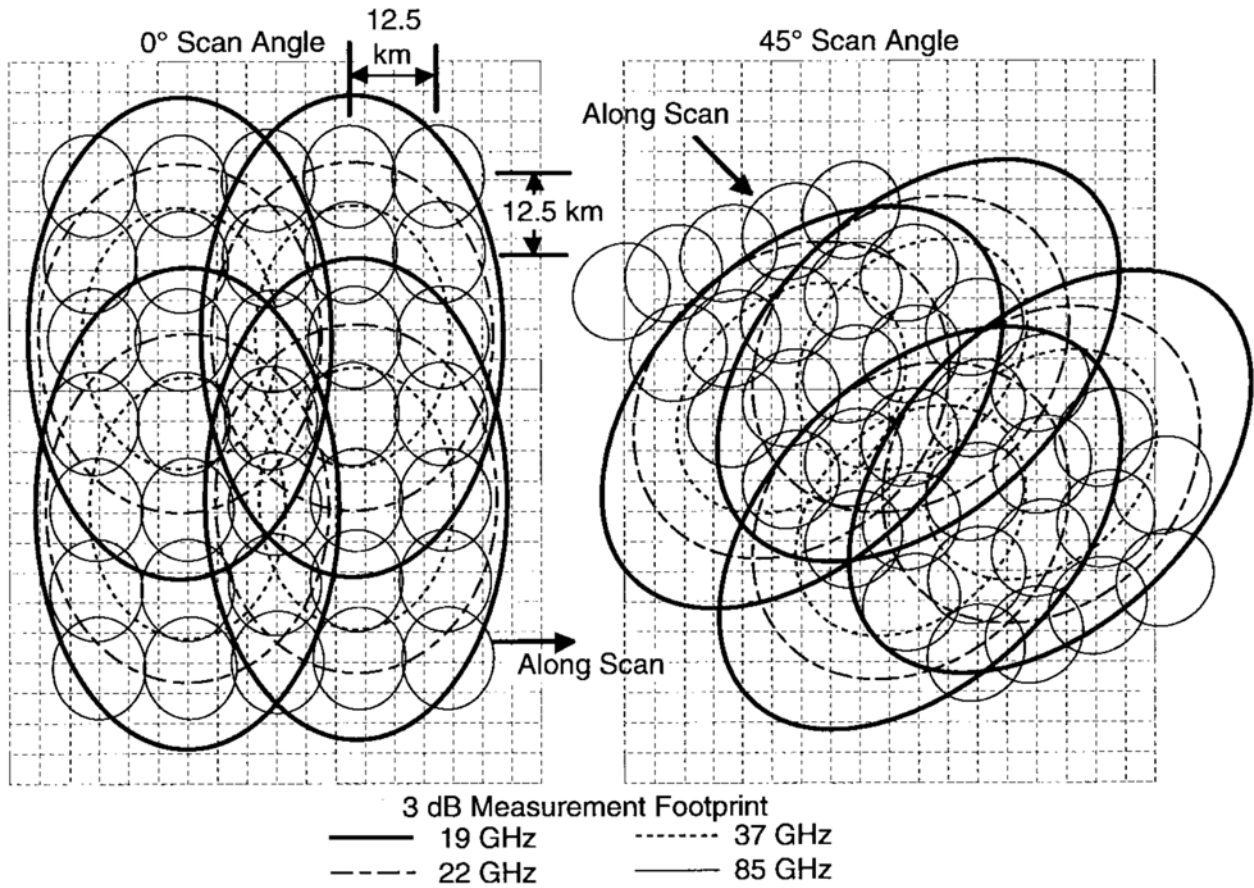
Figure 26: *Illustration of footprints of various channels shown at two scan angles. Only footprints for the V-pol channels are shown. At different scan angles, the footprint orientation changes with respect to the underlying grid (Long and Daum, 1998).*

A.2 SSMIS

The Special Sensor Microwave Imager/Sounder (SSMIS) is a total-power radiometer with 24 operating channels, see Table 11. The antenna rotation rate is 31.6 rpm with measurements collected at a nominal incidence angle of 53.1 $\deg$ producing a nominal swath width of 1700 km and an along-track spacing of nominal 12.5 km. First launched in 2003, SSMIS instruments have flown on multiple spacecraft (F-16, F-17, F-18 and F-19) in the Defense Meteorological Satellite Program (DMSP) F satellite series. The integrate-and-dump filters are 4.2 ms long.

Table 11: *SSMIS channel characteristics (imager channels only) (Kunkee et al., 2008)*

Channel	Center Frequency (GHz)	Bandwidth (MHz)	Footprint (km)
19H	19.35	355	44 x 72
19V	19.35	357	44 x 72
22V	22.235	401	44 x 72
37H	37.0	1615	26 x 44
37V	37.0	1545	26 x 44
91H	85.5	1418	9 x 15
91V	85.5	1411	9 x 15

A.3 SMMR

The Scanning Multichannel Microwave Radiometer (SMMR) instrument is a five frequency Dicke radiometer that first flew on Nimbus-7 and later flew aboard Seasat, both launched in 1978, see Table 12. The inherent resolution of the various SMMR channels varies from a coarse 95 km × 148 km to as fine as 18 km × 27 km depending on frequency (Gloersen and Barath, 1977, Njoku et al., 1980). Satellite altitudes differed by approximately 150 km; the nominal incidence angles were 50 $\deg$ on Nimbus-7 (1978-1987) and 49 $\deg$ on Seasat (1978) with a swath width of 780 km. The antenna rotation rate is 14.6484 rpm.

    The CETB product only includes data from the Nimbus-7 SMMR instrument. The methods described here could be used to reconstruct the Seasat SMMR data.

A.4 AMSR-E and AMSR2

The Advanced Microwave Scanning Radiometer (AMSR) instrument was designed by the Japanese Aerospace Exploration Agency (JAXA) for the ADEOS-II mission. AMSR first flew on ADEOS-II, which operated from January 2003 through October 2003, before the mission

prematurely terminated due to loss of spacecraft power. A second instrument, denoted AMSR-E, was launched aboard the U.S. Aqua mission and operated from May 2002 through 2009. AMSR-E is similar to AMSR but does not include 50 MHz channels (Kawanishi et al., 2003). The nominal incidence angle was 55 $\deg$ with a swath width on AMSR-E of 1450 km. Table 13 describes the primary channels of interest. The nominal rotation rate is 40 rpm, though some data was collected with a rotation rate of 2 rpm. The integrate-and-dump filters are 1.2 ms long for the 89 GHz channels and 2.5 ms long for the other channels.

A.5   WindSat Description

The WindSat/Coriolis mission carries the first orbital polarimetric radiometer (Gaiser et al., 2004). WindSat is designed to evaluate the viability of polarimetric radiometry for measuring the speed and direction of ocean winds from space. WindSat includes multiple polarimetric and dual- polarized channels sharing a 1.8 m offset reflector antenna. The scanning geometry was selected to make both forward and aft-facing brightness temperature measurements over part of its observation swath in order to evaluate the potential of using the azimuth dependence of T_B to retrieve near surface ocean winds from the measurements. The observation swath is illustrated in Figure 27. The nominal incidence angles were 53 $\deg$ for all channels except for the 10.7 GHz channels, which used an incidence angle of 49.9 $\deg$. The channels of interest are described in Table 14. The rotation rate is 31.6 rpm.

The CETB product does not include data from WindSat, but the methods described here could be used to reconstruct WindSat data.
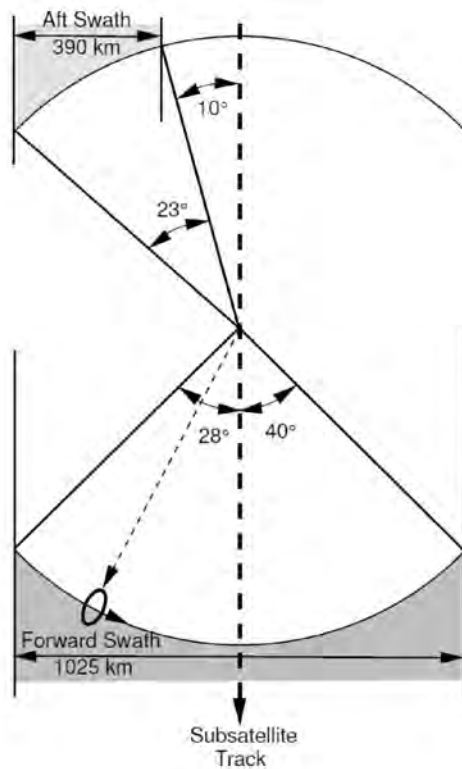
Figure 27: *Illustration of Windsat observation geometry and coverage as seen from above. The antenna helically scans the surface at a constant incidence angle. Observations in the remainder of the azimuth angles are used for calibration.*

Table 12: *SMMR channel characteristics (Gloersen and Barath, 1977). The CETB product includes Nimbus-7 SMMR, not Seasat SMMR.*

Channel	Center Frequency (GHz)	Bandwidth (MHz)	Footprint (km) for Nimbus-7/Seasat
6H	6.63	250	148 x 95 / 121 x 79
6V	6.63	250	148 x 95 / 121 x 79
10.7H	10.69	250	91 x 59 / 74 x 49
10.7V	10.69	250	91 x 59 / 74 x 49
18H	18.0	250	55 x 41 / 44 x 29
18V	18.0	250	55 x 41 / 44 x 29
21H	21.0	250	46 x 30 / 38 x 25
21V	21.0	250	46 x 30 / 38 x 25
37H	37.0	250	27 x 18 / 21 x 14
37V	37.0	250	27 x 18 / 21 x 14

Table 13: *AMSR-E and AMSR2 channel characteristics (Imaoka et al., 2010).*

Channel	Center Frequency (GHz)	Bandwidth (MHz)	Footprint (km) for AMSR-E/AMSR2
6.9H	6.925	350	75 x 43 / 62 x 35
6.9V	6.925	350	75 x 43 / 62 x 35
10.7H	10.65	100	51 x 29 / 42 x 24
10.7V	10.65	100	51 x 29 / 42 x 24
18H	18.7	200	27 x 16 / 22 x 14
18V	18.7	200	27 x 16 / 22 x 14
23H	23.8	400	32 x 18 / 26 x 15
23V	23.8	400	32 x 18 / 26 x 15
36H	36.5	1000	14 x 8 / 12 x 7
36V	36.5	1000	14 x 8 / 12 x 7
89AH	89.0	3000	7 x 4 / 5 x 3
89AV	89.0	3000	7 x 4 / 5 x 3
89BH	89.0	3000	6 x 4 / 5 x 3
89BV	89.0	3000	6 x 4 / 5 x 3

Table 14: *Windsat channel characteristics (Gaiser et al., 2004).*

Channel	Center Frequency (GHz)	Bandwidth (MHz)	Footprint (km)
6.8H	6.8	125	60 x 40
6.8V	6.8	125	60 x 40
10.7H	10.7	300	38 x 25
10.7V	10.7	300	38 x 25
18H	18.7	750	27 x 16
18V	18.7	750	27 x 16
23H	23.8	500	20 x 12
23V	23.8	500	20 x 12
37H	37.0	2000	13 x 8
37V	37.0	2000	13 x 8

B   CETB Projections and Grid Dimensions

There are no changes to the projection and grid definitions between CETBv1 and CETBv2.

Table 15: *CETB product EASE-Grid 2.0 projections and grid dimensions*

Name	Projection	Resolution (km)	Cols	Rows	Latitude Extent	Longitude Extent
EASE2-N25km	Northern Lambert Azimuthal	25	720	720	0°–90°	±180°
EASE2-N12.5km	Northern Lambert Azimuthal	12.5	1440	1440	0°–90°	±180°
EASE2-N6.25km	Northern Lambert Azimuthal	6.25	2880	2880	0°–90°	±180°
EASE2-N3.125km	Northern Lambert Azimuthal	3.125	5760	5760	0°–90°	±180°
EASE2-S25km	Southern Lambert Azimuthal	25	720	720	$-90°$–0°	±180°
EASE2-S12.5km	Southern Lambert Azimuthal	12.5	1440	1440	$-90°$–0°	±180°
EASE2-S6.25km	Southern Lambert Azimuthal	6.25	2880	2880	$-90°$–0°	±180°
EASE2-S3.125km	Southern Lambert Azimuthal	3.125	5760	5760	$-90°$–0°	±180°
EASE2-T25km	Cylindrical Equal-Area	25.02526	1388	540	±67.057 541°	±180°
EASE2-T12.5km	Cylindrical Equal-Area	12.51263	2776	1080	±67.057 541°	±180°
EASE2-T6.25km	Cylindrical Equal-Area	6.256315	5552	2160	±67.057 541°	±180°
EASE2-T3.125km	Cylindrical Equal-Area	3.12815750	11104	4320	±67.057 541°	±180°

C   Implementation Details

The following sections document selected CETB system implementation details.

C.1   End-to-End Swath Overlap

The image reconstruction algorithm requires that input measurements not be duplicated. Where needed, we eliminate end-to-end overlaps as follows:

1. When swath data include a full orbit revolution, we ignore scan lines before or after the integer orbit number of the enclosing file
2. Swath data for half orbit revolutions did not exhibit the overlap issue.

C.2   Approximating the MRF

Reconstruction algorithms require models of the MRF in order to generate enhanced-resolution images. Such models require information about the sensor antenna patterns for each channel. Given the antenna pattern, and information about the rotation rate, the smeared antenna pattern can be computed, from which the MRF is derived. However, in some cases, the amount of information about the detailed antenna pattern is limited (Njoku et al., 1980). In some cases (e.g., SMMR), all that is known is the approximate size of the 1⁄2 power footprint. These elliptical footprints have their semi-major axis along the boresite direction, while the semi-minor axis is in the along-rotation direction. The orientation of the footprint semi-major axis varies with the antenna rotation angle, see Figure 28 and Figure 29.

Lacking a detailed description of the antenna patterns for every sensor, we adopt an approximate model for the MRF based on a rotated, two-dimensional Gaussian function aligned with the footprint orientation, where 1⁄2 power points of the Gaussian correspond to the footprint sizes reported for each sensor. The input data sets do not include the earth azimuth angle explicitly; it is calculated from the spacecraft position and measurement location. It is the angle (on the ground) between the vector defined from the sensor and the measurement center location, relative to true north, and gives the rotation angle of the elliptical footprint relative to north. Based on the sensitivity of the reconstruction when regularization is employed, we find this model to be adequate for our purposes (Long, 2015).

The algorithm for computing the MRF is given here. A grid of pixels centered at the measurement center is defined. The grid size is chosen large enough so that the MRF gain at the edges of the grid is no more than a small threshold, e.g. -30 dB of the MRF peak. Using the map projection, the relative vector distance from the measurement center to the center of each pixel is computed as the vector $\mathbf{X}_{rel} = [x_r, y_r]^T$. This vector is rotated by the
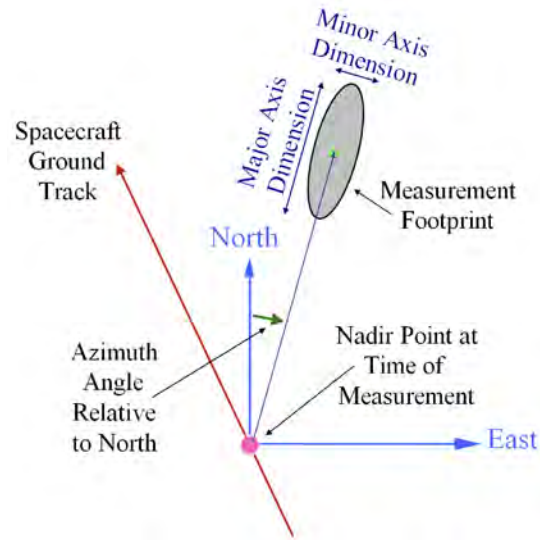
Figure 28: *North-East reference frame for measurement Earth azimuth angle, used to rotate MRF.*
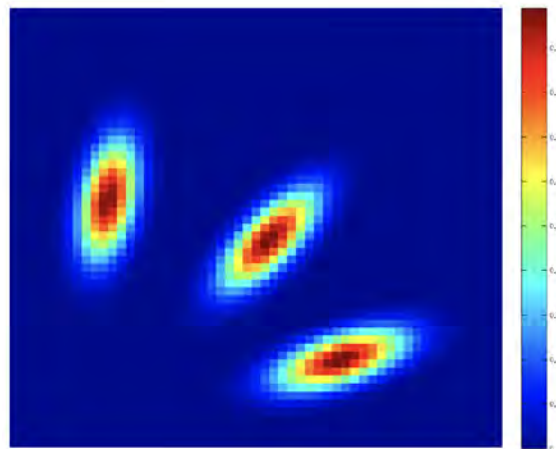

Figure 29: *Illustration of a general Gaussian model for the MRF for a radiometer, in linear space for several antenna rotation angles. The figure is not to scale.*

angle φ relative to north of the ellipse. The rotated system is

$$\mathbf{X} \;=\; [x,y]^T = R(\varphi)\, \mathbf{X}_{rel} \tag{24}$$

where

$$R(\varphi) \;=\; \begin{bmatrix} cos(\varphi) & -sin(\varphi) \\ sin(\varphi) & cos(\varphi) \end{bmatrix} \tag{25}$$

Define the length (in km) of the semi-major axis as L_j and the semi-minor axis as L_n. The MRF gain G at the center of the pixel is then

$$G \;=\; \ln(1/2)\; e^{[(2x/L_j)^2+(2y/L_n)^2]} \tag{26}$$

An example of the result for several values of φ is shown in Figure 29. Note that 1⁄2 power point of G corresponds to the specified ellipse semi-major and semi-minor axes.

This simplified model for the MRF does not exactly model the true MRF (Long, 2015). However, based on the sensitivity of the reconstruction when regularization is employed, this model is adequate for our purposes.

C.3   Determination of Measurements

Each measurement in a swath file is processed onto the underlying grid at a given spatial resolution in the following fashion. A box is defined to be large enough to reasonably include all grid cells that may be affected by the measurement. The MRF is positioned at the nearest grid cell to the measurement location, rotated to the Earth azimuth angle for the measurement, and used to compute the gain response (for that measurement) for each pixel in the box. Each grid cell response is tested to see if it exceeds a threshold and if so, this measurement is used to reconstruct the T_B at the corresponding grid cell. The box size is a function of the semi-major axis of the EFOV (by channel) and the target grid spatial resolution. Through trial-and-error testing with a range of box sizes and SSM/I data, we determined that a box with length of 4-5 times the semi-major axis of the channel EFOV is sufficient to identify all measurements with significant gain. Table 16 lists example CETB box sizes used, by input sensor channel.

Table 16: *Box sizes by sensor and channel used to determine spatial neighborhood for image reconstruction.*

Sensor	Channel (GHz)	EFOV semi–major axis (km)	Box Size (pixels)	rSIR Grid resolution (km)	Box Size (km)	Ratio of Box-size/EFOV semi-major axis
SSM/I	19	69	100 x 100	6.25	625	9.06
	22	60	100 x 100	6.25	625	10.42
	37	37	60 x 60	3.125	187.5	5.07
	85	15	20 x 20	3.125	62.5	4.17
SSMIS	19	72	100 x 100	6.25	625	8.68
	22	72	100 x 100	6.25	625	8.68
	37	44	60 x 60	3.125	187.5	4.26
	91	15	20 x 20	3.125	62.5	4.17
AMSR-E	6	75	24 x 24	12.5	300	4.00
	10	51	20 x 20	12.5	250	4.90
	18	27	22 x 22	6.25	137.5	5.09
	23	32	26 x 26	6.25	162.5	5.08
	36	14	22 x 22	3.125	68.75	4.91
	89A	7	10 x 10	3.125	31.25	4.46
	89B	6	10 x 10	3.125	31.25	5.21
AMSR2	6	61	20 x 20	12.5	250	4.10
	10	42	20 x 20	12.5	250	5.95
	18	22	22 x 22	6.25	137.5	6.25
	23	26	26 x 26	6.25	162.5	6.25
	36	12	24 x 24	3.125	75	6.25
	89	5	20 x 20	3.125	62.5	12.5
SMMR	6	121	120 x 120	12.5	1500	12.40
	10	74	100 x 100	12.5	1250	16.89
	18	44	100 x 100	6.25	625	14.20
	21	38	100 x 100	6.25	625	16.45
	36	21	60 x 60	3.125	187.5	8.93

C.4 Ascending/Descending Classification

CETB files for cylindrical (EASE2-T) grids are classified as "ascending" (A) or "descending" (D) data, which are derived differently, based on the available information in the input swath data as follows:

1. **All sensors except SMMR:** L1C/L1B data for a given scan line are classified as ascending (descending) when the spacecraft latitude of subsequent scan lines is increasing (decreasing).
2. **SMMR:** SMMR Pathfinder data files are packaged into half-orbit swaths that are labeled ascending or descending. This label is assumed to be correct for the half-orbit contents of the file. This classification assumes that the maximum latitude of the target grids is lower than any potential misclassifications of orbital direction for measurements in the same scan line near the poles. The latitude range for the CETB EASE2-T grids is +/-67.06 degrees, so this assumption is reasonable.

CETB files for the azimuthal (Northern, EASE2-N, or Southern, EASE2-S) grids are classified as "morning" (M) or "evening" (E) data, which are derived from measurements that are classified using the local time-of-day (ltod) criteria, described in Section 6.6.

C.5 Measurement Incidence and Azimuth Angles

The CETB incidence angle for a given grid cell is calculated as the average incidence angle of component measurements used for the reconstructed TB. We investigated sample SSM/I data over Greenland and the Amazon, looking for a potential first-order correction to T_B as a function of incidence angle. We found no relationship independent of satellite orbital direction and concluded that there is no simple systematic correction for incidence angle. We therefore did not use incidence angle in the T_B image reconstruction. We include as a CETB file variable the average incidence angle for the set of contributing measurements for each pixel, for potential use by producers of derived geophysical products. We note that for a particular sensor the incidence angle variation is small.

The input incidence angles for the CETB are derived differently, based on the available information in the input swath data, as follows:

1. **All sensors except SMMR:** L1C/L1B swath data include incidence angle for every measurement in the swath file.
2. **SMMR:** SMMR Pathfinder data files only include 30 "Footprint incidence angle" values across each scan that contained 90 measurements. Incidence angles are linearly interpolated across the scan, using the provided angles.

The measurement azimuth angle is used in CETB image reconstruction to rotate the modeled spatial response function to determine the appropriate weight of each measurement affecting a given grid cell. Neither L1C/L1B nor SMMR Pathfinder data include the

required azimuth angle; however, both include spacecraft position by scanline and measurement location. The azimuth angle is derived from these locations as the bearing with respect to true north at the measurement location of the vector from the spacecraft position to the measurement position.

C.6   Exclusion of Selected Measurements

In most cases, only the highest-quality input measurements are used for the image reconstruction. Highest quality was dependent on the input data producer quality flags, but differed by input data as follows:

1. **All sensors except SMMR:** L1C/L1B swath measurements were used if none of the quality flags were nonzero, with the exception of Cautionary flag values 1 (`Possible sunGlint, 0 le sunGlintAngle lt 20` and 4 (`Data corrected for warm load instrusion`) (PPS, 2023). Examination of selected subsets of data indicated that including pixels with flag value 1 avoided producing images with significant missing areas in the Southern Hemisphere. Likewise, flag value 4 are also included in image reconstruction, since it is indicated as both cautionary and corrected by the L1C data producers. Rather than producing no data for these conditions, we chose to allow image reconstruction from measurements if either of cautionary quality flag 1 or 4 were set.
2. **SMMR:** SMMR Pathfinder data were used if none of the quality bits were set, with the exception of bit 4, documented as `large deviations in incidence angles on adjacent scan lines`, and bit 5, documented as `sun-in-the-cold-horn` period. Analysis of SMMR Pathfinder data indicated that bit 4 affected less than 1% of scan lines. We decided to include data with this issue because it was only flagging a potential incidence angle deviation. Initial processing that excluded data for which bit 5 had been set resulted in significant areas of missing gridded data at high latitudes in the Southern Hemisphere. For data affected by the bit 5 problem, SMMR Pathfinder documentation indicated that cold calibration counts may have been interpolated and brightness temperature calibration accuracy may have been reduced (Njoku et al., 1998). Rather than producing no data for these locations, we chose to allow image reconstruction from SMMR measurements if either of quality bit 4 or bit 5 were set.

C.7   Hole Artifacts in Reconstructed Images

When no swath measurement center locations map to the area of a gridded pixel, GRD images occasionally include single pixels with no data. Normally, rSIR images do not suffer from this problem, because the rSIR gain threshold is set to a value that almost always ensures at least one component measurement that can be used to derive the pixel brightness temperature.

For most of the CETB input data, we determined that a gain threshold value of -8 dB was sufficient for image reconstruction. However, with this threshold, the relatively small footprint size for all sensor channels above 85 GHz occasionally produced image artifacts as undesirable holes, where no measurements were mapped to an output pixel location. To mitigate this artifact and produce a continuous field of output brightness temperatures, we increased the gain threshold to -12 dB for the following channels: AMSR-E 89 GHz, SSM/I 85 GHz and SSMIS 91 GHz. We increased the gain threshold to -16 dB for AMSR2 89 GHz. The actual value used to produce the T_B variable in a given file is stored in the T_B variable metadata field, `measurement_response_threshold_dB`.

Beginning with AMSR-E data on 04 Nov 2004, the 89 GHz A-horn exhibited a permanent problem that resulted in a loss of observations from this horn for the remainder of the AMSR-E lifespan (Beitsch et al., 2014). Even with the larger gain threshold, the rSIR 3.125 km 89 GHz data after this date may occasionally have missing pixels.

C.8   Known Periods of Missing Observations

To indicate that a known period with no observations has been intentionally produced, CETB files are created for every day and channel during sensor nominal lifetime. If an entire image is missing data, the file is produced with variable arrays set to the value of the variable `_FillValue`. During a given sensor lifetime, there should be no missing files for individual dates.

In April, 2016, the 37V channel on F17–SSM/I experience high noise levels that appeared to improve in May 2016, but continued intermittently beginning in August 2016 (Personal communication, Dr. Wes Berg, June, 2020). These noisy periods are flagged in L1C quality data and excluded from CETB images.

C.9   Deprecated `missing_value` Variable Attribute

CETBv1 files included variable attributes `_FillValue` and `missing_value` that were assigned distinct values. The `_FillValue` was used to identify pixels that were initialized but never assigned a value. Examples include: "corner" pixels at locations in the opposing hemisphere in the azimuthal grids; or pixels where no swath data measurements were assigned on a given day. The distinct `missing_value` identified pixels where the calculated T_B was outside of the variable `valid_range`.

If only one missing value is needed for a variable, the CF conventions (Eaton et al., 2021) recommend that this value be specified using the `_FillValue` attribute. User feedback on CETBv1 files indicated that the special `missing_value` attribute condition was confusing and did not really need to be distinguished from the conditions flagged by the `_FillValue`. Therefore, CETBv2 files no longer use the `missing_value` attribute. The `_FillValue` is used in all variable arrays to indicate any pixels with missing values, regardless of the reason.

D   CETBv2 Data Definition

D.1   File Requirements

Following are requirements for CETBv2 files:

- Output file format shall be acceptable for NSIDC DAAC to easily ingest to ECS
- File size maximum will be $< 1\,\mathrm{GB}$ (larger files are allowed in ECS, but fast network speeds cannot always be assumed)
- Files will conform to netCDF-CF 1.9 conventions (Eaton et al., 2021); this is a change from CF 1.6 (Eaton et al., 2011) used for CETBv1, it allows us to continue our practice that does not bloat file sizes by including lat/lon arrays in each file, which was technically a non-compliant aspect of CF-1.6 files, but is now tolerated in CF-1.9
- Files will include CF-compliant coordinate variables with projected coordinate locations
- Files should pass CF-compliance-checking required by the NSIDC DAAC
- Each file will contain 1 T_B array variable, with associated ancillary variables, possibly different variable attributes appropriate for each gridding technique. We may have a practical limit on the number of ancillary variables to include, limited by maximum file size
- Each file of the same type (GRD or rSIR) will contain the same file-level metadata for that type. e.g. an rSIR file T_B variable will contain different variable attributes from those in a GRD file, but all rSIR files will contain consistent metadata
- We will follow the DRY (Don't Repeat Yourself) principle: Metadata will not be duplicated at multiple places in the same file (there are a few notable exceptions to this, discussed in Brodzik et al. (2018))
- DRY exception: Time values will be machine- and human-readable
- DRY exception: Some projection metadata may be in multiple forms (CF-compliant attributes, a proj4 string and/or a WKT string that repeat the same projection definition)
- Variable/attribute names will be CF-compliant whenever possible

The CETBv2 .nc files work with gdal utility, *gdal_translate*, to produce a geoTIFF version of each of the data variables <varName> in the file, (details in Brodzik et al. (2018)), for e.g.:

```
gdal_translate -of GTiff -b 1 NETCDF:"cetb.nc":<varName> <cetb.varName>.tif
```

D.2   Filename Convention

CF-compliant *CETBv2* data files are distributed by the NSIDC DAAC (`http://nsidc.org/data/nsidc-0630`). The filenaming convention has changed from CETBv1. CETBv2 file-

name lengths are shorter than CETBv1 lengths, with parts re-ordered to conform to current DAAC requirements. The format of the date string has changed from year and day-of-year to year, month, day. The part separator has been changed from hyphen to underscore, and the *input_source* has been removed, because it is included in the file-level metadata. With a few exceptions to update global attribute `geospatial_bounds_crs` values and deprecation of the `missing_value` variable attribute, the remainder of the file contents are unchanged from the *CETBv1* contents described in Brodzik et al. (2018).
The CETBv2 filename convention is:

productId_algorithm_gridName_platformSensor_pass_channel_yyyymmdd_version.nc

where parts of the filename are described in Table 17.

Table 17: *CETBv2 file naming convention.*

Part	Description	Values
productId	NSIDC unique data product id	NSIDC0630
algorithm	Image reconstruction algorithm	one of: GRD or SIR
gridName	EASE-Grid 2.0 grid id	e.g. EASE2_N25km, see Column 1 of Table 15
platformSensor	Satellite platform and sensor	one of: • NIMBUS7 • F[08|10|11|13|14|15]_SSMI • F[16|17|18|19]_SSMIS • AQUA_AMSRE • GCOMW1_AMSR2
pass	Pass direction (T grids) or ltod (N or S)	one of: • A = Ascending • D = Descending • M = Morning • E = Evening
channel	Channel (frequency in GHz and polarization)	multi-digit frequency and 1-letter polarization, differs by sensor, e.g. 37H
yyyymmdd	Date	4-digit year, 2-digit day-of-year, 2-digit day-of-month
version	Major.Minor version number	e.g. v2.0
.nc	file format	NetCDF file formatting

E   Local Time-of-Day Divisions

The following plots summarize ltod analysis, by sensor and (where necessary) year used to determine temporal divisions in "morning" vs. "evening" images. All plots are derived using observations between 70 and 71 N/S latitudes. Plots for sensors whose ltod did not change significantly are only included for one representative year.
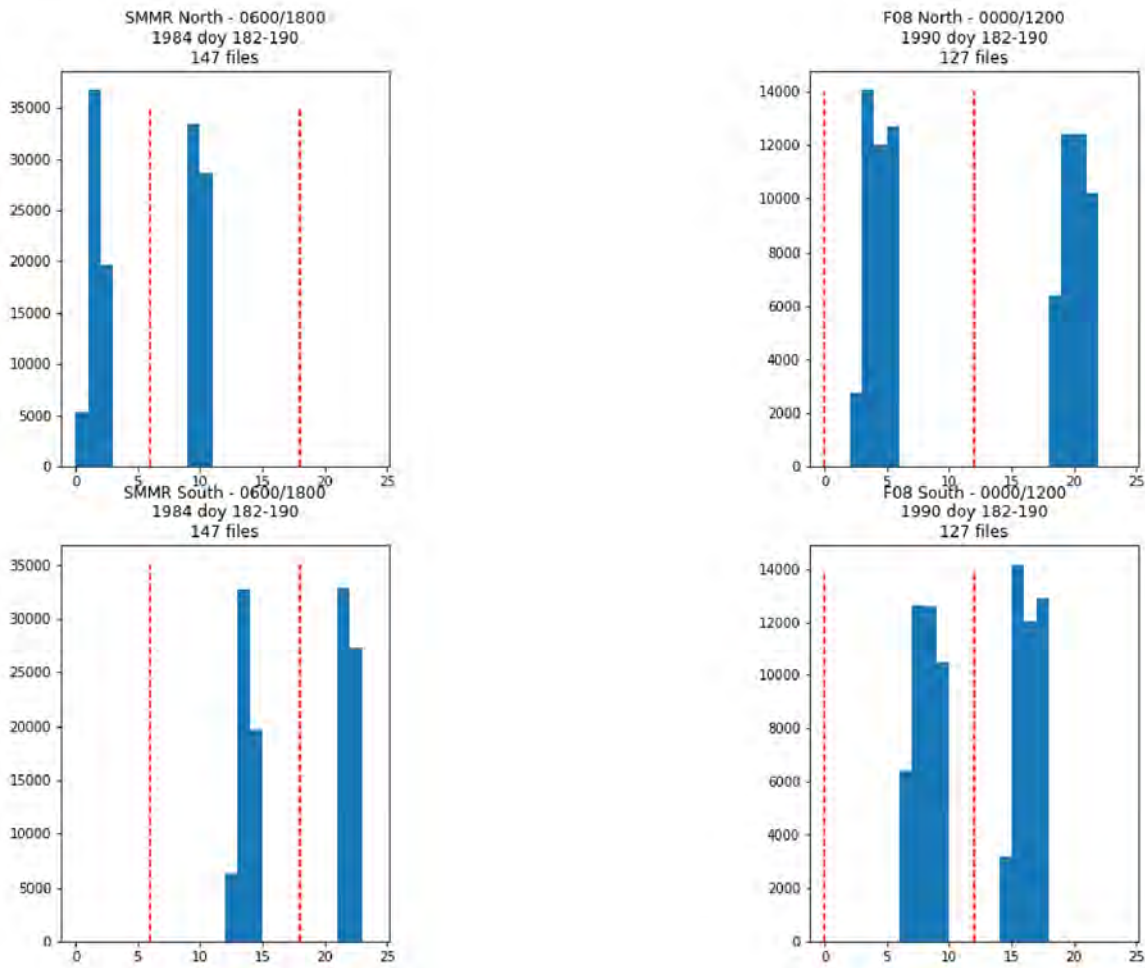
Figure 30: *SMMR (left) and F08 (right) ltod bounds for 1984 and 1990, respectively. There was no signficant drift in ltod over the lifetime of these sensors.*
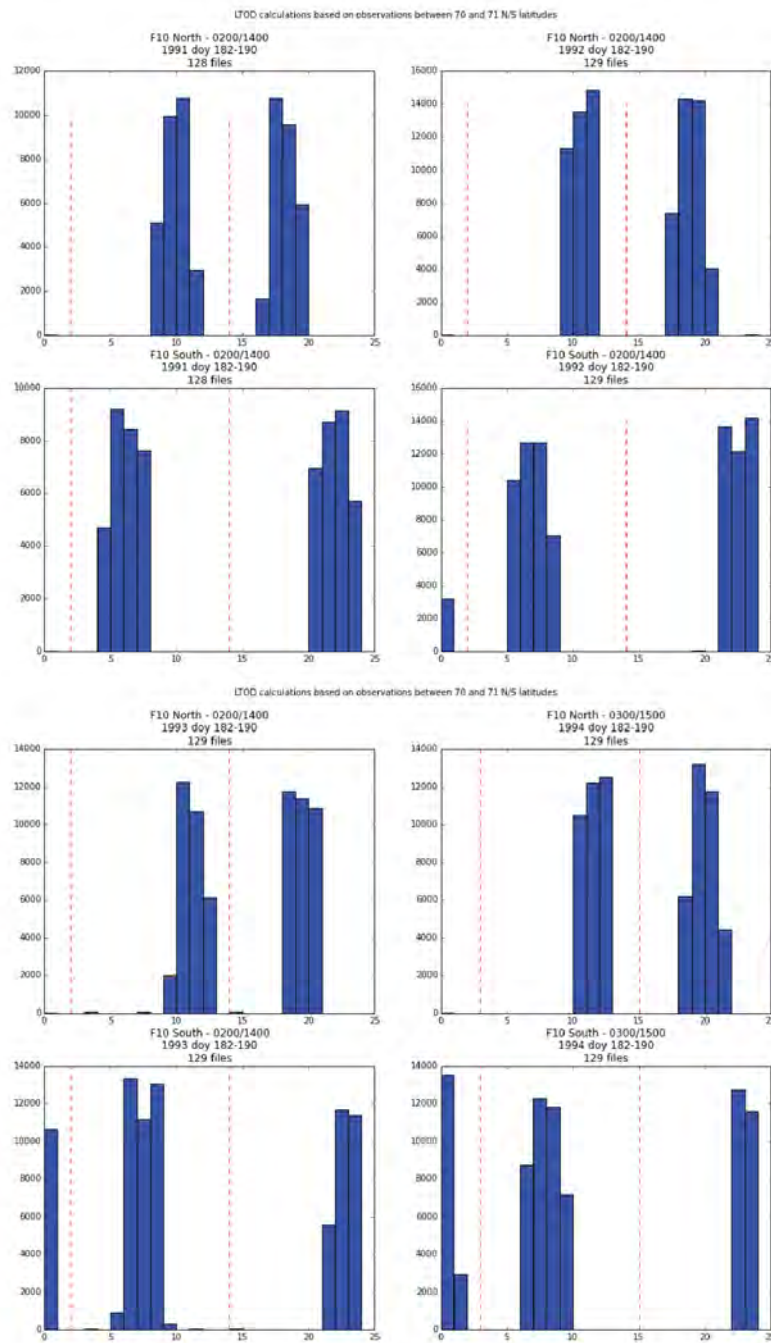
Figure 31: *F10 ltod bounds for 1991-1994. The F10 ltod times shifted once (from 1993-1994), during the lifespan of this sensor.*
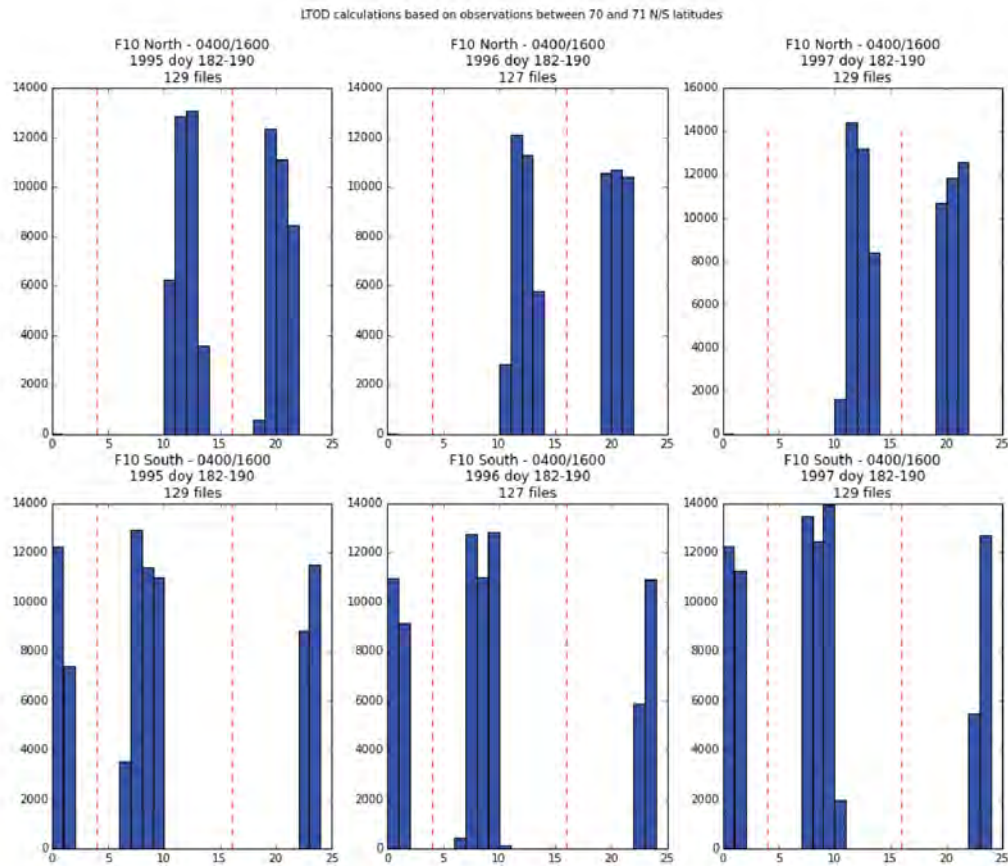
Figure 32: *F10 ltod bounds for 1995-1997. The F10 ltod times shifted once (from 1993-1994), during the lifespan of this sensor.*
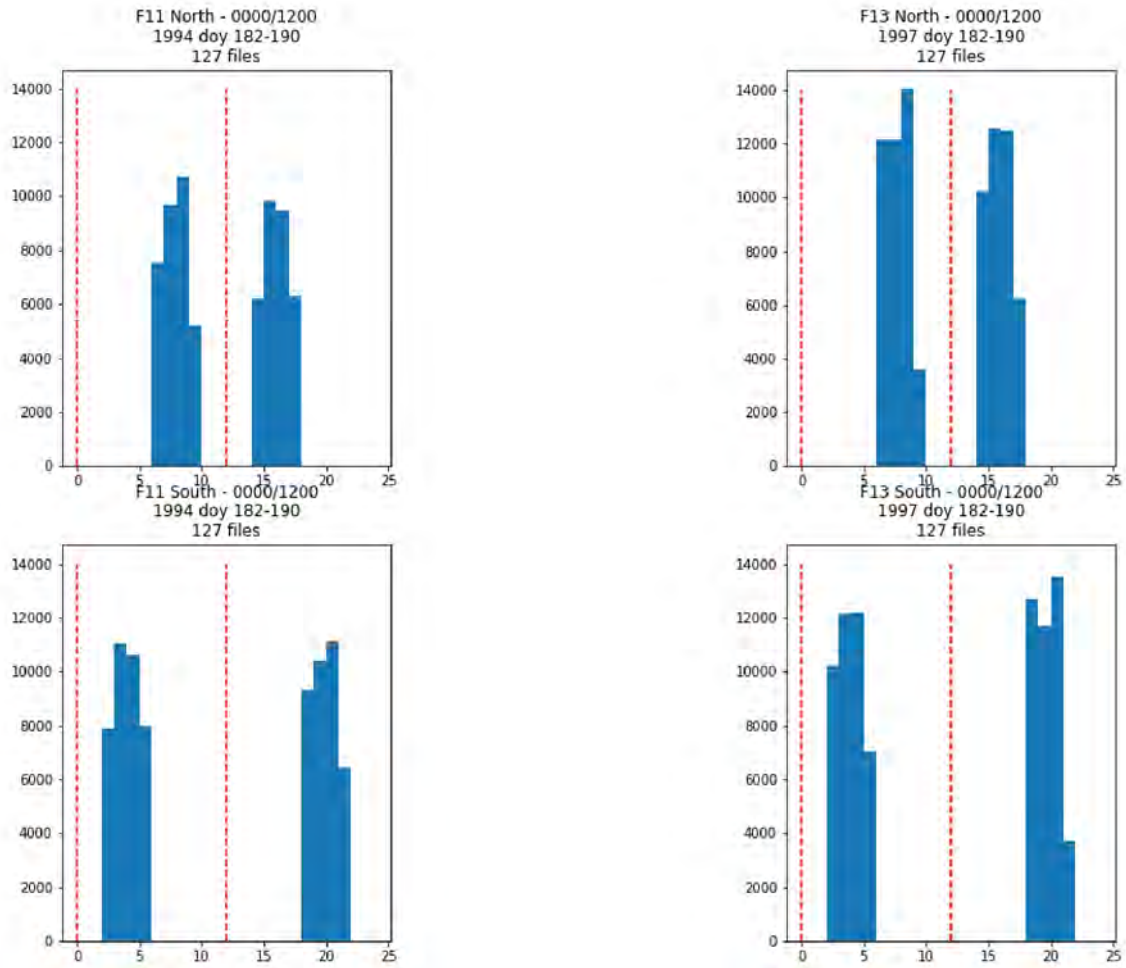
Figure 33: *F11 (left) and 13 (right) ltod bounds for 1994 and 1997, respectively. There was no signf-icant drift in ltod over the lifetime of these sensors.*
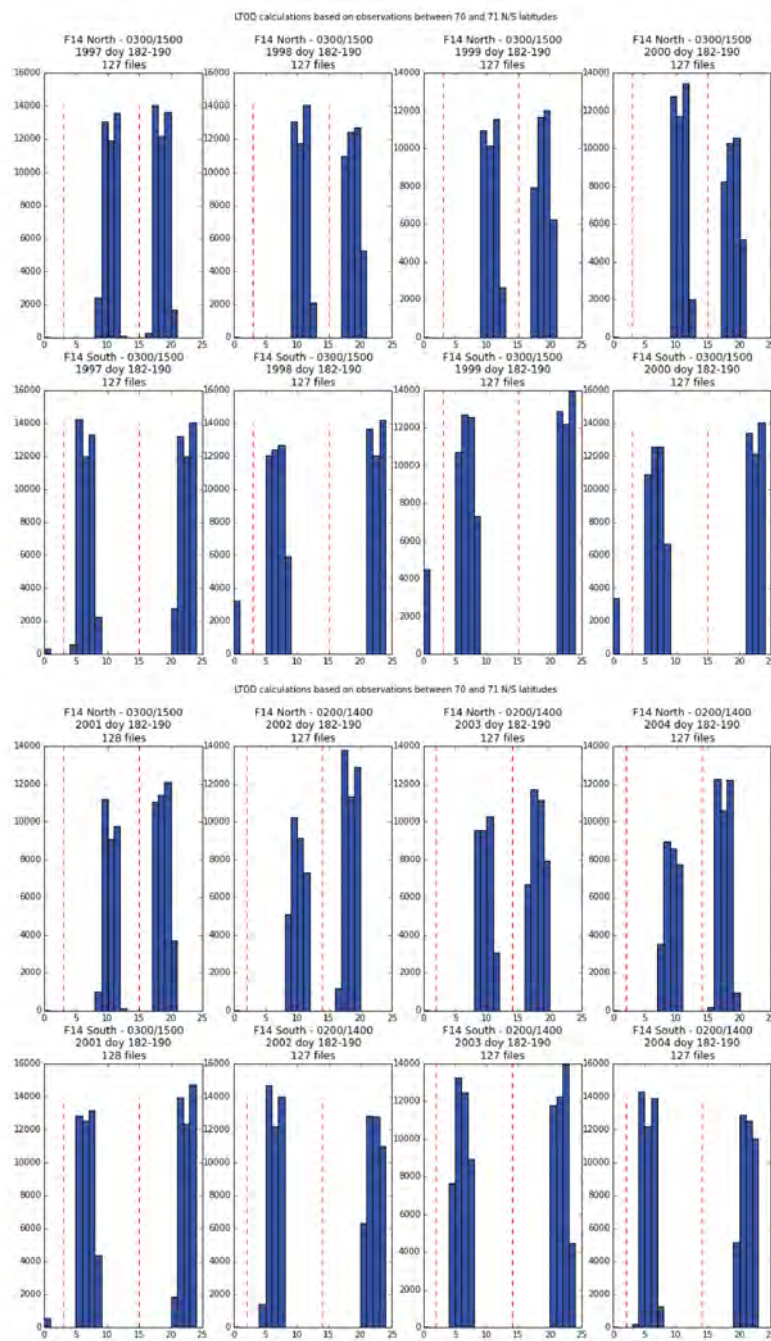
Figure 34: *F14 ltod bounds for 1997-2004. The F14 ltod times shifted twice (from 2001 to 2002 and again from 2004 to 2005), during the lifespan of this sensor.*
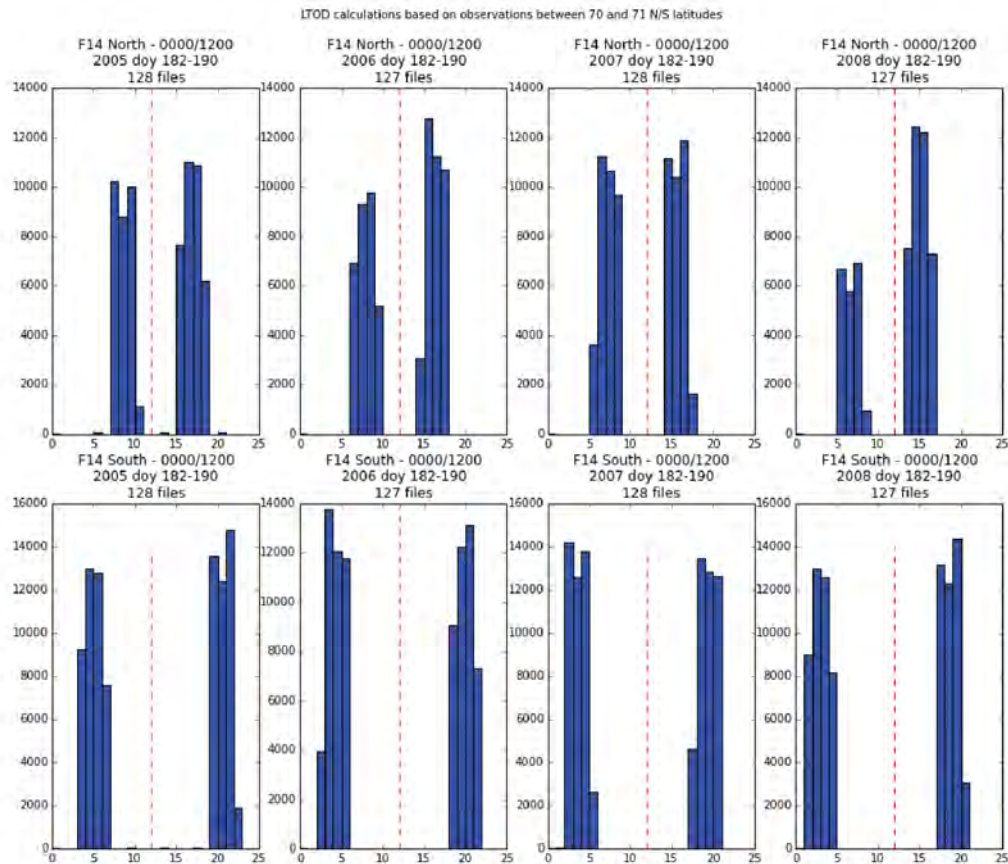
Figure 35: *F14 ltod bounds for 2005-2008. The F14 ltod times shifted twice (from 2001 to 2002 and again from 2004 to 2005), during the lifespan of this sensor.*
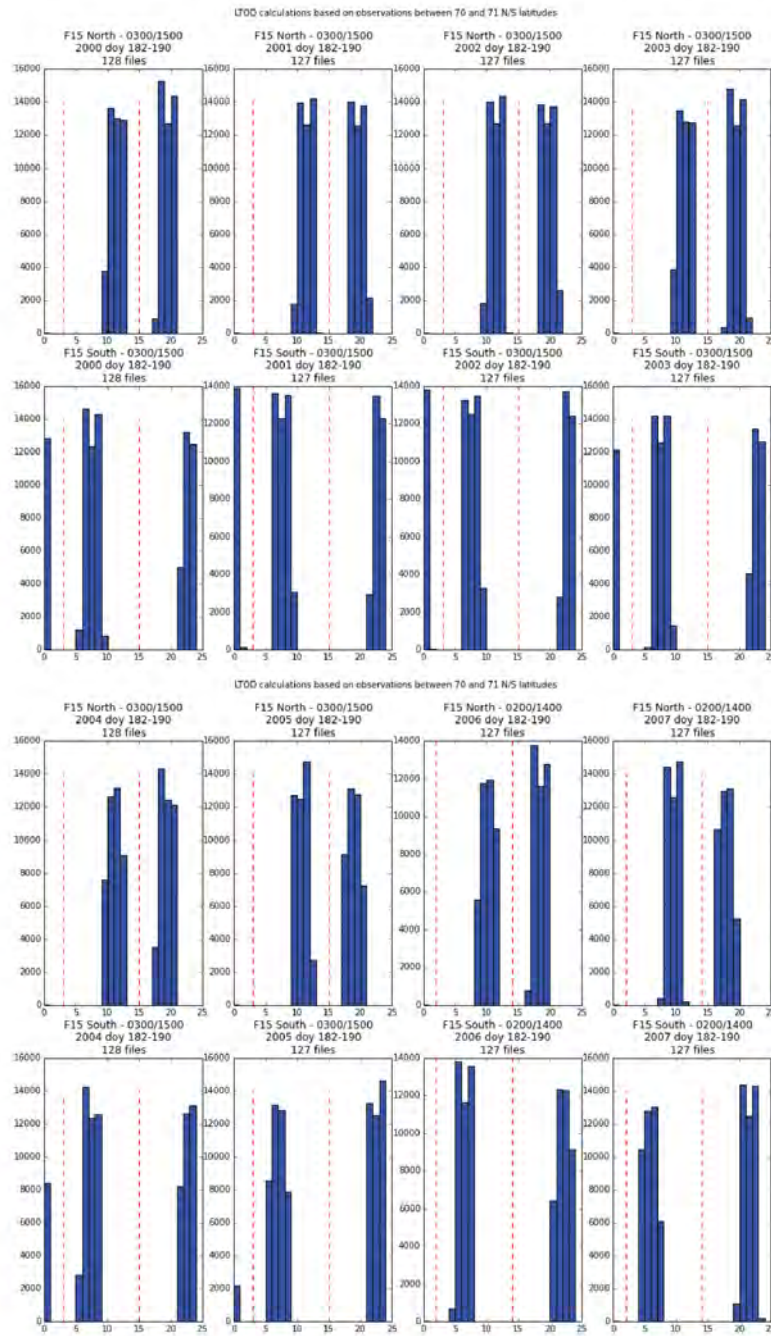
Figure 36: *F15 ltod bounds for 2000-2007. The F15 ltod times shifted several times during the lifespan of this sensor.*
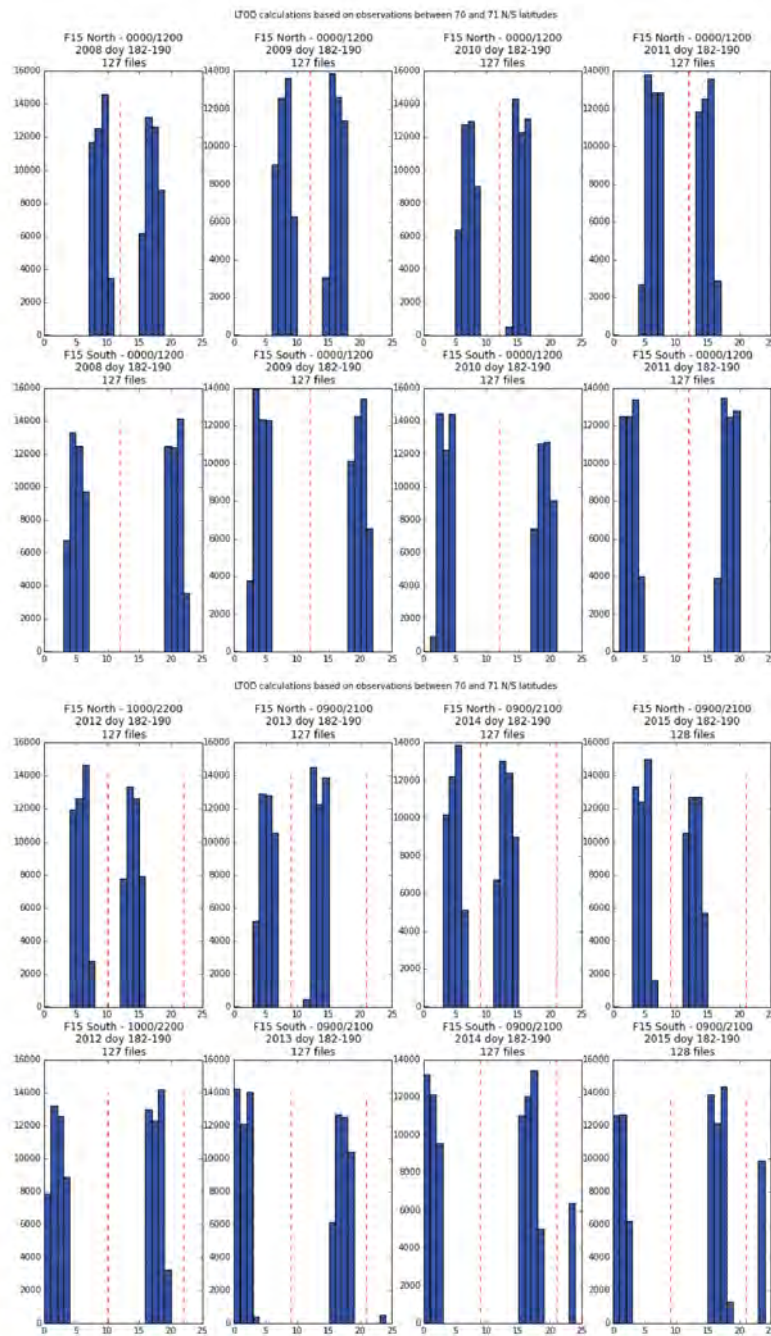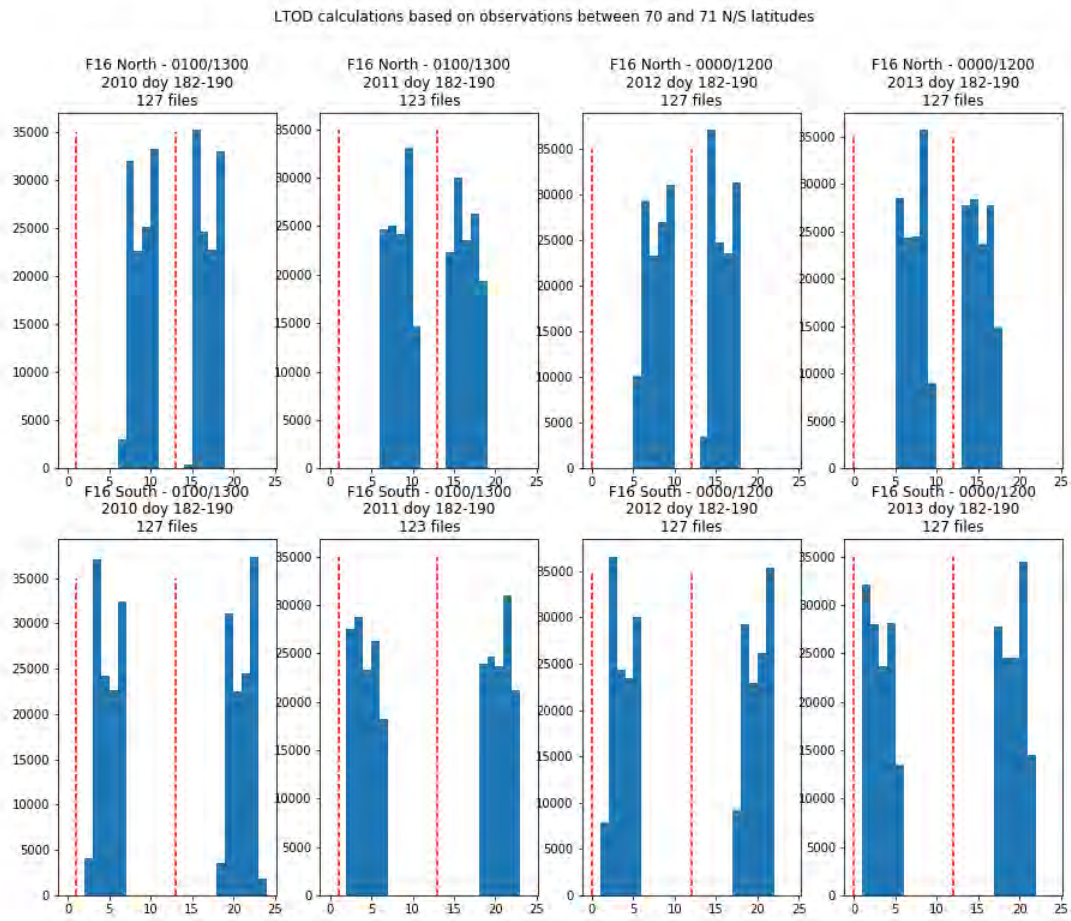
Figure 37: *F15 ltod bounds for 2008-2015. The F15 ltod times shifted several times during the lifespan of this sensor.*
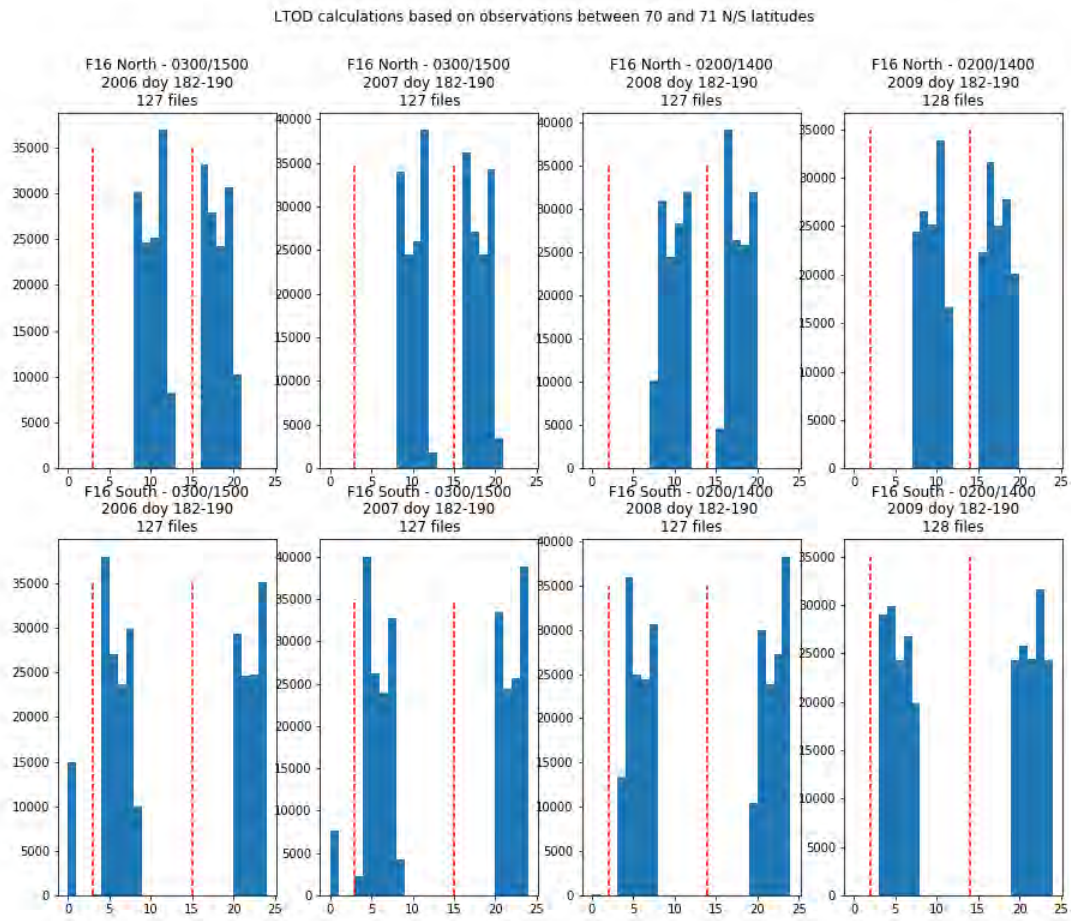
Figure 38: *F16 ltod bounds for 2006-2009. The F16 ltod times shifted several times during the lifespan of this sensor.*

Figure 39: *F16 ltod bounds for 2010-2013. The F16 ltod times shifted several times during the lifespan of this sensor.*
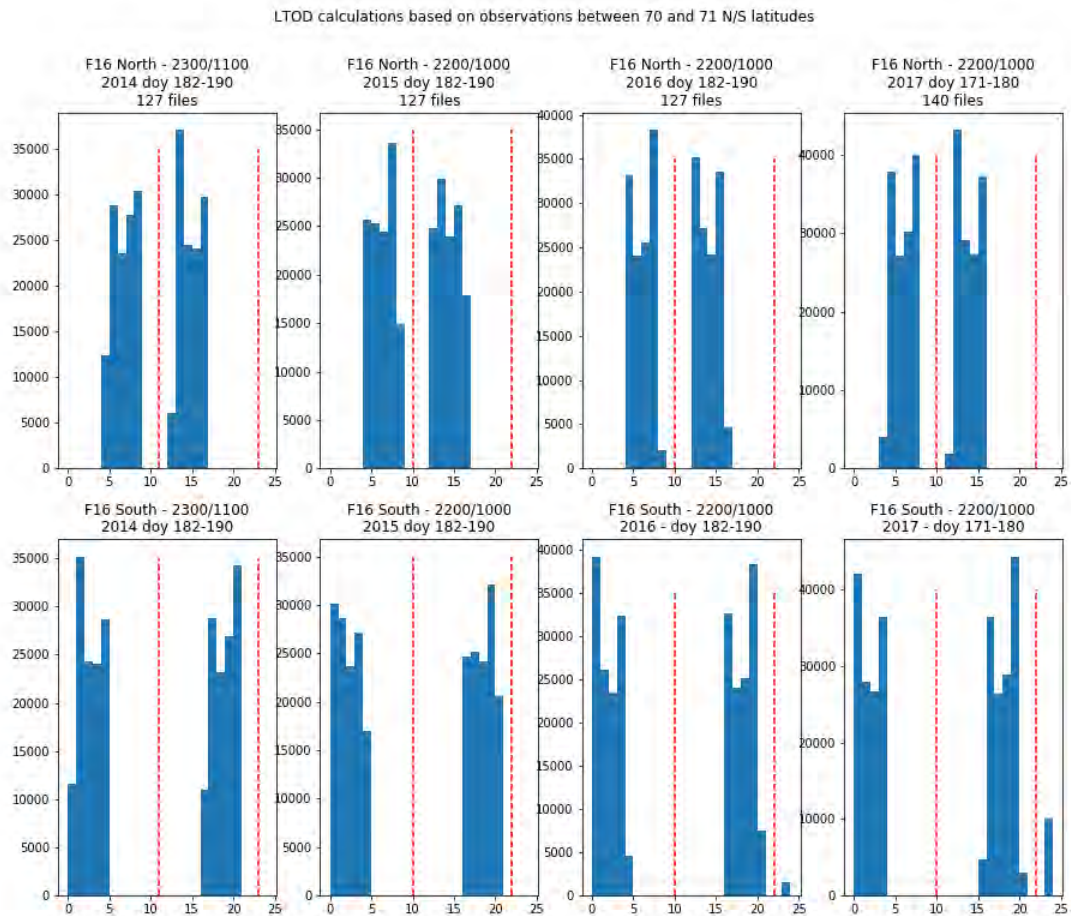
Figure 40: *F16 ltod bounds for 2014-2017. The F16 ltod times shifted several times during the lifespan of this sensor.*
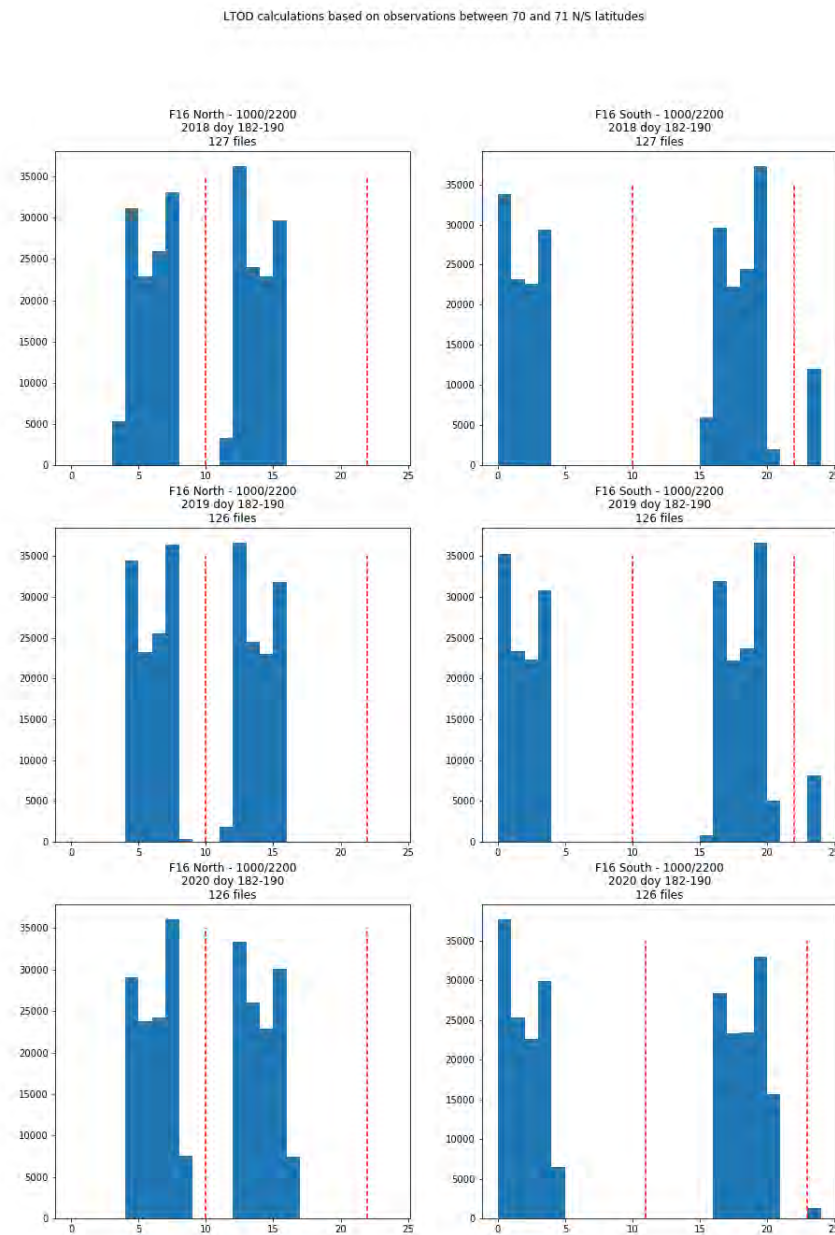
Figure 41: *F16 ltod bounds for 2018-2020. The F16 ltod times shifted several times during the lifespan of this sensor.*
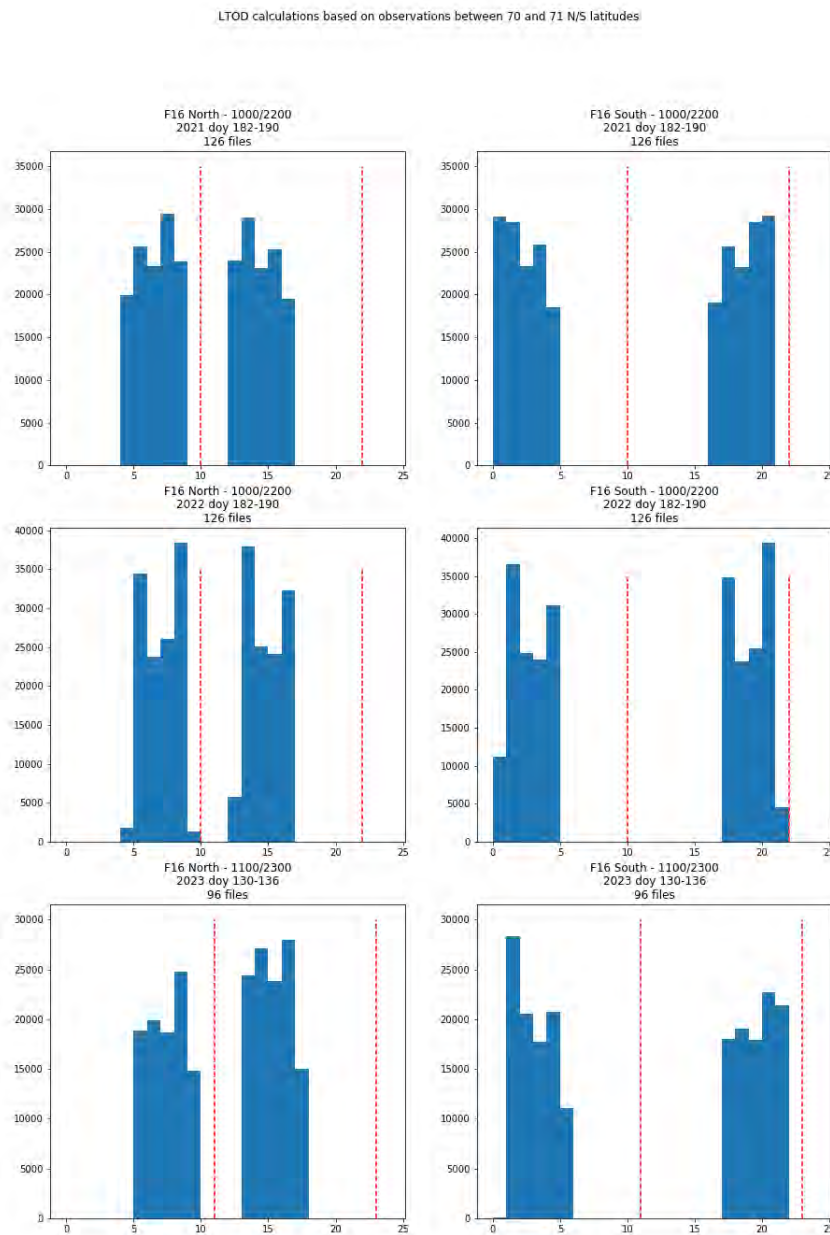
Figure 42: *F16 ltod bounds for 2021-2023. The F16 ltod times shifted several times during the lifespan of this sensor.*
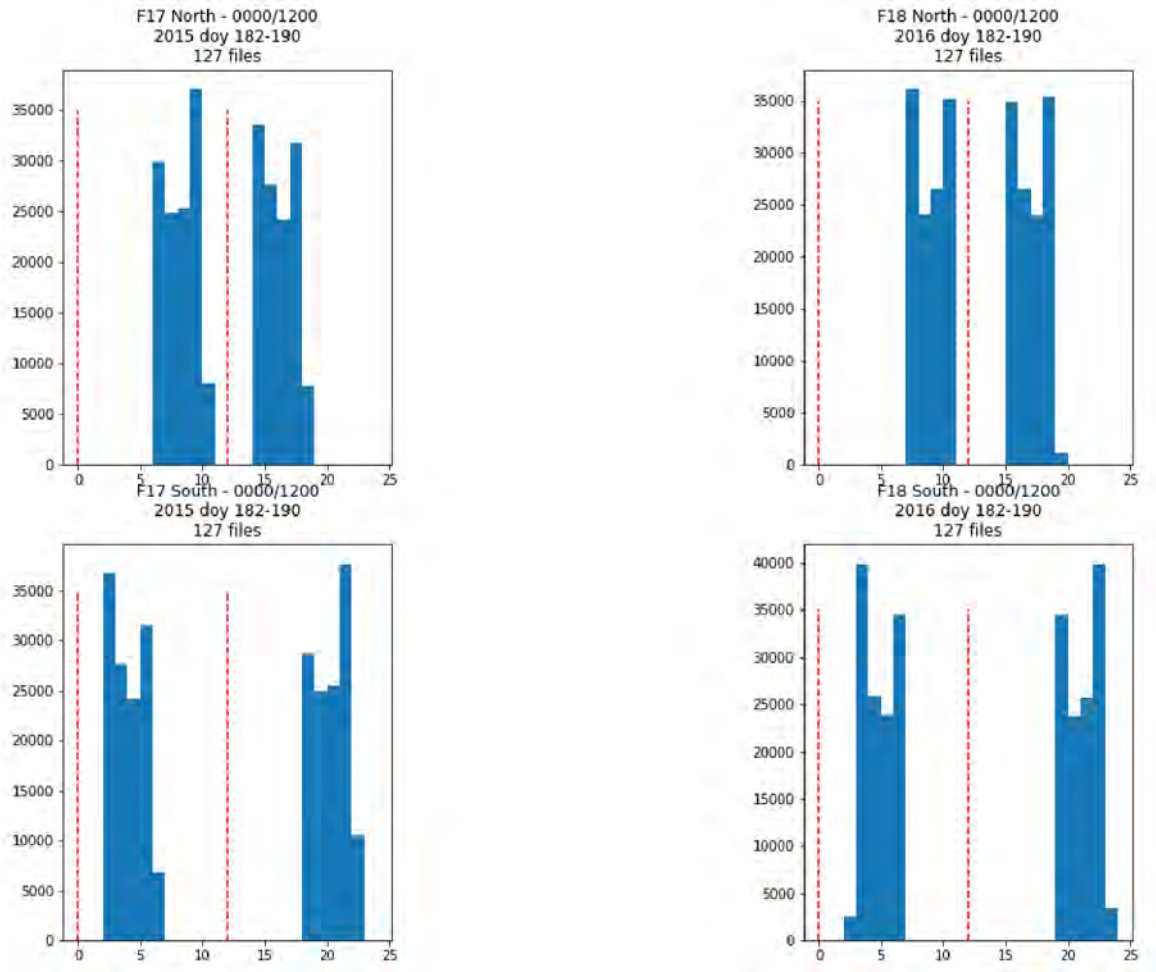
Figure 43: *F17 (left) and F18 (right) ltod bounds for 2015 and 2016, respectively. There has been no significant drift in ltod over the lifetime of these sensors so far.*
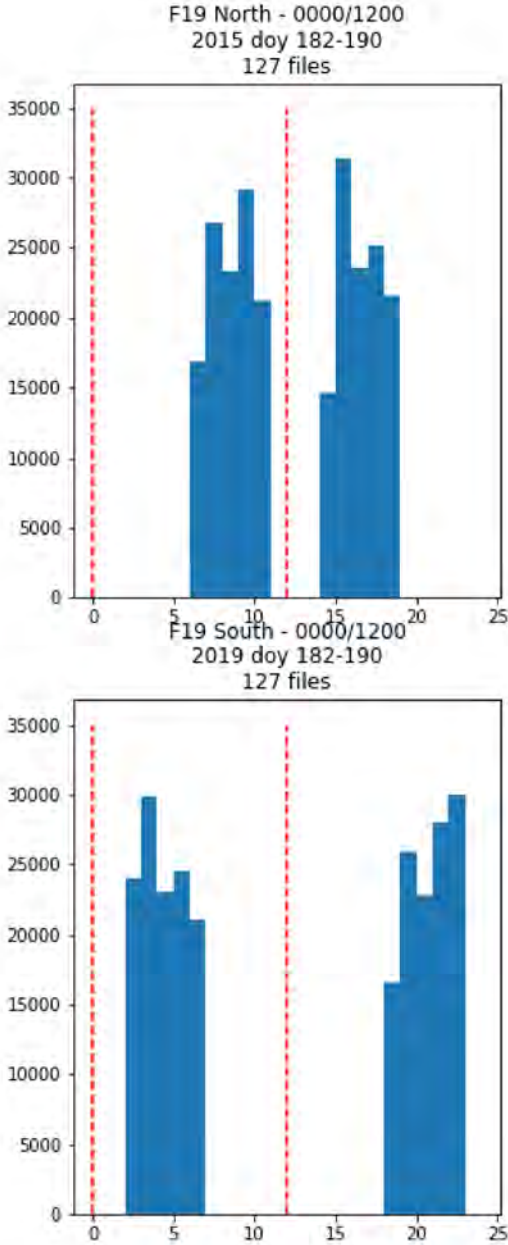
Figure 44: *F19 ltod bounds for 2015. There was no significant drift in ltod over the lifetime of this sensor.*
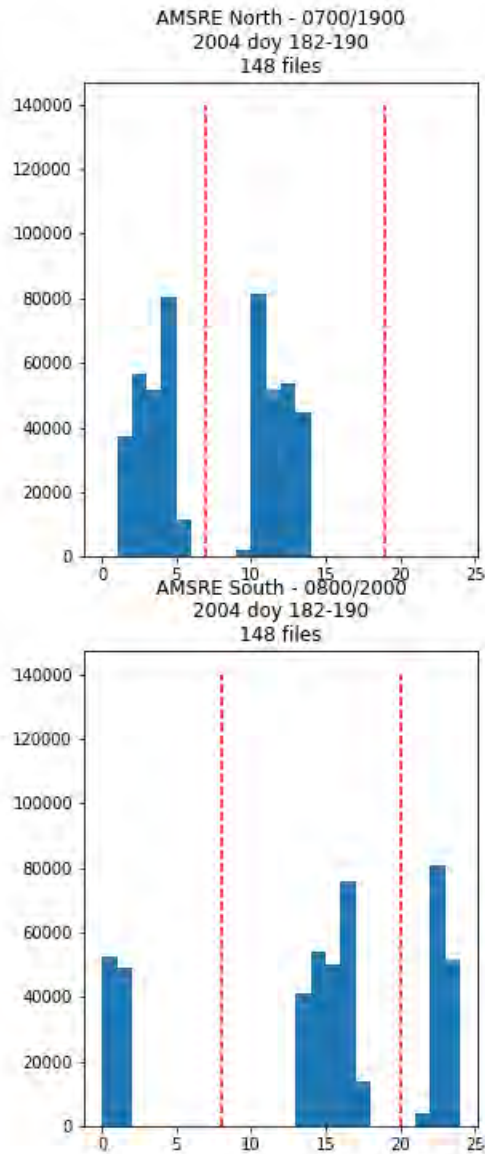
Figure 45: *AMSR-E ltod bounds for 2004. There was no significant drift in ltod over the lifetime of this sensor.*
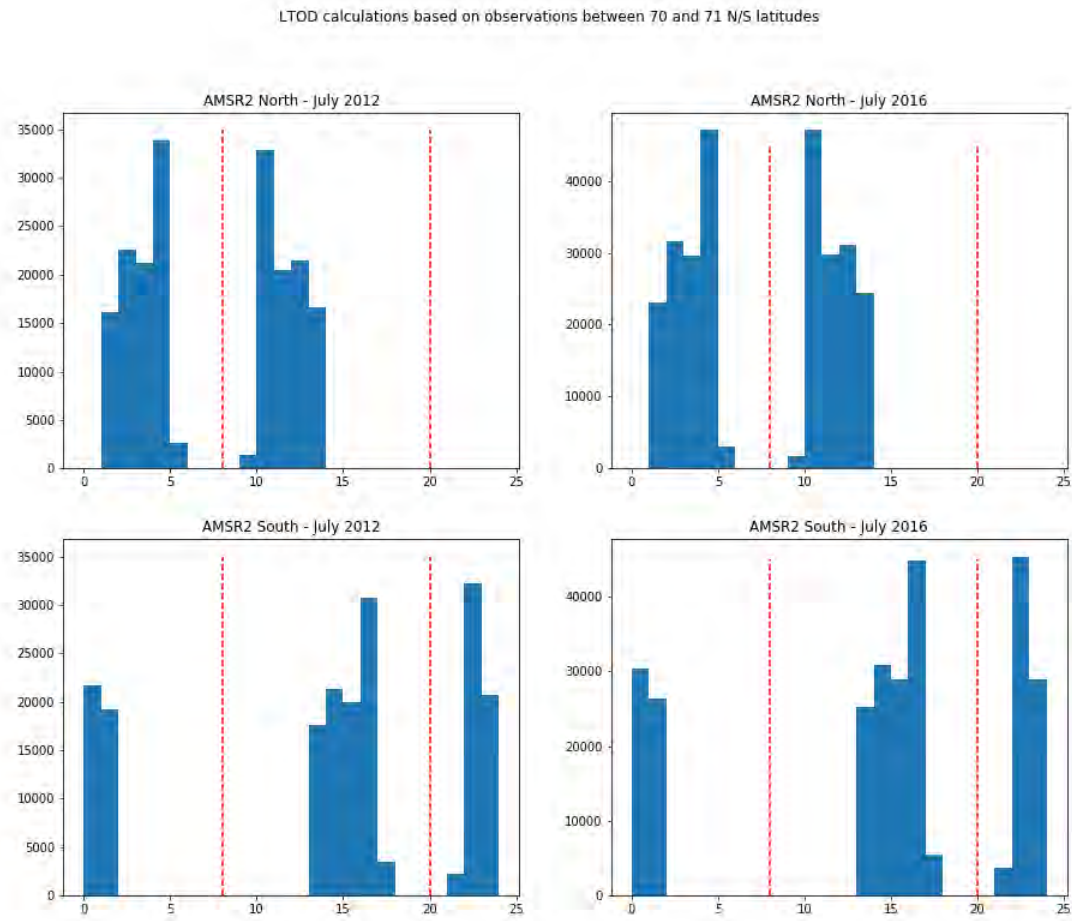
Figure 46: *AMSR2 ltod bounds for 2012 and 2016. There has been no significant drift in ltod over the lifetime of this sensor.*

F   Acronyms and Abbreviations

Table 18: *List of Acronyms and Abbreviations*

AMSR-E	Advanced Microwave Scanning Radiometer - Earth Observing System
ATBD	Algorithm Theoretical Basis Document
BG	Backus-Gilbert
BYU	Brigham Young University
CDR	Climate Data Record
CETB	Calibrated Passive Microwave Daily EASE-Grid 2.0 Brightness Temperature
CF	Climate and Forecast Metadata Conventions
DAAC	Distributed Active Archive Center
dB	decibel
DIB	Drop-in-the-bucket averaging (used to produce GRD products)
DMSP	Defense Meteorological Satellite Program
EASE-Grid	Equal-Area Scalable Earth Grid (Original Definition)
EASE-Grid 2.0	Equal-Area Scalable Earth Grid Version 2.0
EASE2-M	EASE-Grid 2.0, Mid- and Low-Latitude Cylindrical Projection
EASE2-N	EASE-Grid 2.0, Northern Hemisphere Projection
EASE2-S	EASE-Grid 2.0, Southern Hemisphere Projection
EASE2-T	EASE-Grid 2.0, Temperate and Tropical Cylindrical Projection
ECS	EOSDIS Core System
EIA	Earth Incidence Angle
EOSDIS	Earth Observing System Data and Information System
EPSG	European Petroleum Survey Group
ERDC	Engineer Research and Development Center
ESDR	Earth System Data Record
FCDR	Fundamental Climate Data Record
GHz	GigaHertz
GMI	GPM Microwave Imager
GPM	Global Precipitation Mission
GRD	(Drop-in-the-bucket) Gridding Method
JAXA	Japanese Aerospace Exploration Agency
JPSS	Joint Polar Satellite System
L1C	Level 1C
ltod	Local Time-of-Day
MEaSUREs	Making Earth System Data Records

	for Use in Research Environments
MRF	Measurement Response Function
NASA	National Aeronautics and Space Administration
NOAA	National Oceanic and Atmospheric Administration
NORAD	North American Aerospace Defense Command
NSIDC	National Snow and Ice Data Center
NetCDF	Network Common Data Format
NRT	Near real-time
PPS	Precipitation Processing System
rSIR	Radiometer version of SIR
RTM	Radiative Transfer Model
SCP	Scatterometer Climate Record Pathfinder
SDR	Sensor Data Record
SIR	Scatterometer Image Reconstruction
SMMR	Scanning Multichannel Microwave Radiometer
SSM/I	Special Sensor Microwave/Imager
SSMIS	Special Sensor Microwave Imager Sounder
T_B	brightness temperature
TBD	To be determined
TLE	Two-Line Element
UCB	University of Colorado at Boulder
UTC	Coordinated Universal Time